Effects of Cubic Hardening Nonlinearities on the Flutter of a Three Degree of Freedom Airfoil

Udbhav Sharma

gte271u@mail.gatech.edu

School of Aerospace Engineering

Georgia Institute of Technology

05/05/05

Abstract

This paper derives nonlinear second order ordinary differential equations describing the motion of a two dimensional airfoil allowing for three spatial degrees of freedom in the airfoil's angular rotation, vertical movement, and control surface rotation. The equations of motion are derived from the Euler-Lagrange equation with the dissipative forcing functions arising from two dimensional aerodynamics incorporating results from Theodorsen's unsteady thin airfoil theory. A particular type of structural nonlinearity is included by using cubic polynomials for the stiffness terms. The resulting nonlinear model predicts damped, exponentially decreasing oscillations below a critical airflow speed called the flutter boundary. The paper shows how this speed can be predicted from the eigenvalues of the corresponding linear system. By changing certain airfoil geometrical and mechanical properties, it is demonstrated that it is possible to aeroelastically tailor the airfoil such that flutter is avoided for a given flight regime. Above the flutter speed, limit cycle oscillations are predicted that grow in amplitude with the airspeed. The amplitude of the limit cycles are also dependent on the position of the elastic center and the magnitude of the cubic hardness coefficient term.

1 Introduction

Aeroelastic considerations are of vital importance in the design of aerospace-craft because vibration in lifting surfaces, called flutter, can lead to structural fatigue and even catastrophic failure [1]. An important problem concerns the prediction and characterization of the so called flutter boundary (or speed) in aircraft wings. Classical aeroelastic theories [2] predict damped, exponentially decreasing oscillations for an aircraft surface perturbed at speeds below the critical flutter boundary. Exponentially increasing oscillations are predicted beyond this speed [3]. Therefore, knowledge of the stability boundary is vital to avoid hazardous flight regimes. This stability problem is studied in classical theories with the governing equations of motion reduced to a set of linear ordinary differential equations [2].

Linear aeroelastic models fail to capture the dynamics of the system in the vicinity of the flutter boundary. Stable limit cycle oscillations have been observed in wind tunnel models [3] and real aircraft [1] at speeds near the predicted flutter boundary. These so called benign, finite amplitude, steady state oscillations are unfortunately not the only possible effect. Unstable limit cycle oscillations have also been observed not only *after* but also *before* the onset of the predicted flutter speed [3]. In the case of unstable limit cycle oscillations the oscillations grow suddenly to very large amplitudes resulting in catastrophic flutter and structural failure. A more accurate aeroelastic model is needed to incorporate the nonlinearities present in the system to account for such phenomena.

Nonlinear effects in aeroelasticity can arise from either the aerodynamics of the flow or from the elastic structure of the airfoil. Sources of nonlinearity in aerodynamics include the presence of shocks in transonic and supersonic

flow regimes and large angle of attack effects, where the flow becomes separated from the airfoil surface. Structural nonlinearities are known to arise from freeplay or slop in the control surfaces, friction between moving parts, and continuous nonlinearities in structural stiffness [3].

In the paper, we first adopt a linear aerodynamic model that limits the ambient airflow to inviscid, incompressible (low Mach number), and steady state flow. A more sophisticated aerodynamic model using Theodorsen's unsteady thin airfoil theory is then used to capture dissipative effects in flutter. We derive the structural equations separately from the aerodynamics because it is simple to adopt more sophisticated aerodynamics at a later stage without affecting the structural model. Further development includes the addition of nonlinear polynomial terms to model structural stiffness once the unsteady model is in place.

2   The Airfoil Cross-Section

The physical model used to study aeroelastic behavior of aircraft lifting surfaces has traditionally been the cross section of a wing (or other lifting surface). This 2-dimensional (2D) cross section is called a typical airfoil section [2]. The flow around this section is assumed to be representative of the flow around the wing. Because the airfoil section is modeled as a rigid body, elastic deformations due to structural bending and torsion are modeled by springs attached to the airfoil [1]. The use of an airfoil model is consistent with standard aerodynamic analysis, in which the flow over 3-dimensional (3D) lifting surfaces is first studied using a 2D cross section and the results are then suitably modified to account for 3D (finite wing) effects [4]. In this study, finite wing corrections are not incorporated into

the aerodynamic model.

A brief discussion of airfoil terminology will be useful at this point. The tip of the airfoil facing the airflow is called the leading edge (LE) and the end of the airfoil is called the trailing edge (TE). The straight line distance from the LE to the TE is called the chord of the airfoil. The airfoil chord is fixed by the type of airfoil specified, given by standard National Advisory Committee for Aeronautics (NACA) nomenclature [5] and hence can be used as a universal reference length. The mean camber line is the locus of points midway between the upper and lower surfaces of the airfoil. For a symmetric airfoil, the mean camber line is coincident with the chord line.

The typical airfoil section studied in this paper includes a TE control surface known as a flap (see Figures 1(a) and (b)). As an airfoil moves through a flow, it has potentially an infinite number of spatial degrees of freedom (DOF). Here, the airfoil is constrained to one translational and two rotational DOF (see Figure 1(a)). The translational DOF called plunging is the vertical movement of the airfoil about the local horizontal with a time dependent displacement $h = h(t)$. The rotational or pitching DOF of the airfoil about the elastic center (point 3 in Figure 1(a)) is represented by the angle $\alpha = \alpha(t)$ measured counterclockwise from the local horizontal. Finally, the rotational or flapping DOF of the flap about its hinge axis (point 6 in Figure 1(a)) is measured by the angle $\beta = \beta(t)$ with respect to the airfoil chord line. The elastic constraints on the airfoil are represented by one translational and two rotational springs with stiffness coefficients k_h, k_α and k_β, treated for now as constants, but developed further subsequently.

Points of interest on the airfoil section are shown in Figure 1(b). The center of pressure for the airfoil lies at point 1 (see section 5 for further information). In the case of a thin symmetric airfoil the center of pres-
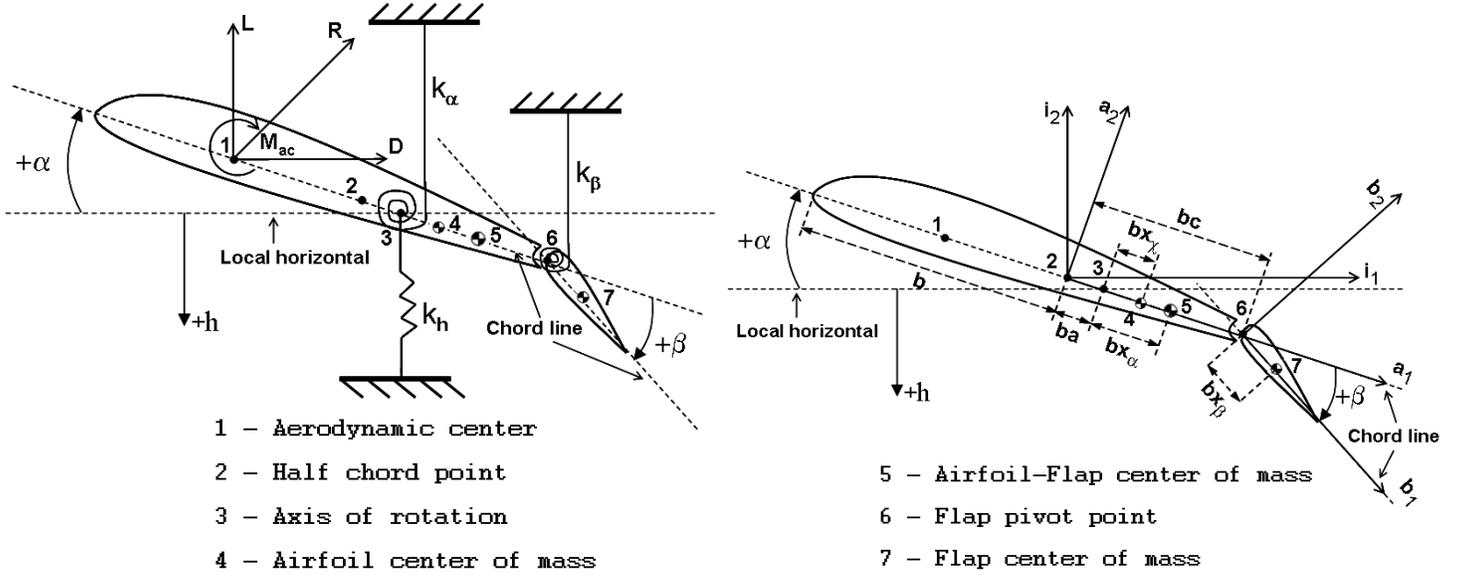
Figure 1: (a) Typical airfoil section (cross-section of a wing) showing aerodynamic forces lift L, drag D, the resultant force R and resultant torque M_{ac}, and elastic constraints k_α, k_β, and k_h. (b) Same airfoil section showing inertial axes $(I(\hat{i}_1, \hat{i}_2, \hat{i}_3))$ and airfoil-fixed axes $(A(\hat{a}_1, \hat{a}_2, \hat{a}_3)$ & $B(\hat{b}_1, \hat{b}_2, \hat{b}_3))$, and constants $(a, b, c, x_\alpha, x_\beta$ & $x_\chi)$. Points of interest 1–7 are shown. See Table 1 for definitions.

sure is coincident with the aerodynamic center of the airfoil. Point 2 is the half chord point of the airfoil section. One half of the chord length (b in Figure 1(b)) is used in this paper to non-dimensionalize the other geometrical lengths of the airfoil. The half chord is also used as the characteristic length of an airfoil for the purpose of formulating the aerodynamic forces and torques (see section 5). Two important reference points are the elastic center, point 3, about which the airfoil rotates and the flap hinge location, point 6, about which the TE flap rotates. The center of gravity (CG) of the

4

airfoil is located at point 4 and that of the flap is at point 7. The CG of the airfoil-flap combination is located at point 5. The geometrical constants relating these points are defined graphically in Figure 1(b) and summarized in Table 1.

3 Equations of Motion

The classical aeroelastic equations of motion for a typical airfoil section were derived by Theodorsen [2] using a force balance. The equations are re-derived in this paper by writing Euler-Lagrange equations of motion for each DOF. The aerodynamic force and torques (see section 4) associated with the airfoil are treated as external forces. Three Cartesian coordinate frames are used in the following derivation - an inertial frame $I(\hat{i}_1, \hat{i}_2, \hat{i}_3)$ with its origin at the half chord and two airfoil fixed frames. The first airfoil-fixed frame $A(\hat{a}_1, \hat{a}_2, \hat{a}_3)$ also has its origin at the airfoil half chord. The points of interest 1–6 in Figure 1(b) on the chord line are coincident with the $\hat{a}_1$ direction. The second non-inertial frame $B(\hat{b}_1, \hat{b}_2, \hat{b}_3)$ has its origin at the flap pivot point with the flap center of mass lying in the $\hat{b}_1$ direction. The $\hat{a}_1$ and $\hat{b}_1$ axes are coincident with the inertial $\hat{i}_1$ axis for the airfoil in its non-deflected position. The general rotations to transform a vector $\vec{v}$ from frames A, B into the inertial reference frame I are [6],

$$\{\vec{v}\}_I = [\mathbf{R}_z(-\alpha)]\{\vec{v}\}_A \quad \text{and} \quad \{\vec{v}\}_I = [\mathbf{R}_z(-\alpha - \beta)]\{\vec{v}\}_B \tag{1}$$

where $[\mathbf{R}_z(\psi)]$ is the Euler rotation matrix given by,

$$[\mathbf{R}_z(\psi)] = \begin{bmatrix} \cos(\psi) & \sin(\psi) & 0 \\ -\sin(\psi) & \cos(\psi) & 0 \\ 0 & 0 & 1 \end{bmatrix}$$

5

We note that the rotations are considered small and hence small angle approximations are used (i.e. $\sin(x) \approx x$ and $\cos(x) \approx x$).

The Lagrangian is the difference between the kinetic $\mathcal{T}$ and potential $\mathcal{V}$ energies of the system, $\mathcal{L} = \mathcal{T} - \mathcal{V}$. By defining the gravitational potential datum line at the $\hat{i}_1$ inertial axis (see Figure 1(b)) and arguing that the movement of the CG of the airfoil about this line is small, the contribution of gravitational potential to the energy of the system can be neglected [1]. The potential energy of the system is then,

$$\mathcal{V} = \frac{1}{2}k_\alpha\,\alpha^2 + \frac{1}{2}k_\beta\,\beta^2 + \frac{1}{2}k_h\,h^2 \tag{2}$$

The expression for the kinetic energy in terms of the velocities v_j, $j = \{4, 7\}$ of the mass centers (points 4 and 7 in Figure 1(b)) and the angular rotations α and β is

$$\mathcal{T} = \frac{1}{2}I_a\,\dot{\alpha}^2 + \frac{1}{2}I_f\,(\dot{\alpha} + \dot{\beta})^2 + \frac{1}{2}m_a\,\vec{v}_4 \cdot \vec{v}_4 + \frac{1}{2}m_f\,\vec{v}_7 \cdot \vec{v}_7 \tag{3}$$

Here, m_a is the mass of the entire airfoil, m_f is the mass of the flap alone, and I_j, $j = \{a, f\}$ are the corresponding moments of inertia with respect to the CG locations.

The velocities of the mass centers can be written relative to the rotation centers (points 3 and 6 in Figure 1(b)) as,

$$\begin{aligned} \vec{v}_4 &= \vec{v}_3 + (-\dot{\alpha})\hat{a}_3 \times \vec{r}_{34} \\ \vec{v}_7 &= \vec{v}_6 + (-\dot{\beta})\hat{b}_3 \times \vec{r}_{67} + (-\dot{\alpha})\hat{a}_3 \times \vec{r}_{36}. \end{aligned} \tag{4}$$

The length of the vectors $\vec{r}_{ij}$ can be obtained from Figure 1(b). Performing rotations into the inertial reference frame using equation (1) with small angle

6

approximations and taking the cross products in the above equation,

$$\vec{v}_4 = -[bx_\chi \alpha \, \dot{\alpha}] \, \hat{i}_1 - [\dot{h} + bx_\chi \, \dot{\alpha}] \, \hat{i}_2$$

$$\vec{v}_7 = -[bx_\beta(\alpha + \beta) \, \dot{\beta} + b(c - a)\alpha \, \dot{\alpha}] \, \hat{i}_1 - [\dot{h} + bx_\beta \, \dot{\beta} + b(c - a) \, \dot{\alpha}] \, \hat{i}_2.$$

Recalling that α and β are small, we keep only the terms that are linear in α and β in the above equation,

$$\vec{v}_4 \cdot \vec{v}_4 = |\vec{v}_4|^2 = (\dot{h} + bx_\chi \, \dot{\alpha})^2$$

$$\vec{v}_7 \cdot \vec{v}_7 = |\vec{v}_7|^2 = (\dot{h} + bx_\beta \, \dot{\beta} + b(c - a) \, \dot{\alpha})^2. \tag{5}$$

Substituting equations (5) into the kinetic energy expression from (3) yields,

$$
\begin{aligned}
\mathcal{T} = {} & \frac{1}{2} \left[I_a + I_f + m_a b^2 x_\chi^2 + m_f b^2 (x_\beta + c - a)^2 \right] \dot{\alpha}^2 + \frac{1}{2} \left[I_f + m_f b^2 x_\beta^2 \right] \dot{\beta}^2 + \\
& + \frac{1}{2} \left[m_a + m_f \right] \dot{h}^2 + \left[I_f + m_f b^2 x_\beta^2 + (m_f b^2 x_\beta)(c - a) \right] \dot{\alpha}\dot{\beta} + \\
& + \left[m_a b x_\chi + m_f b(x_\beta + c - a) \right] \dot{h}\dot{\alpha} + m_f b x_\beta \, \dot{\beta}\dot{h}
\end{aligned}
\tag{6}
$$

We note here that from Figure 1(b) the CG location of the airfoil-flap combination can be expressed in terms of the CG locations of the airfoil and flap as $(m_a + m_f)bx_\alpha = m_a bx_\chi + m_f b(x_\beta + c - a)$. Then, the following structural quantities that appear in Theodorsen's form of the equations [2] are defined as follows:

$$
\begin{aligned}
m &= m_a + m_f \\
I_\alpha &= I_a + I_f + m_a b^2 x_\chi^2 + m_f b^2 (x_\beta + c - a)^2 \\
I_\beta &= I_f + m_f b^2 x_\beta^2 \\
S_\alpha &= m_a b x_\chi + m_f b(x_\beta + c - a) = (m_a + m_f)bx_\alpha = mbx_\alpha \\
S_\beta &= m_f b x_\beta.
\end{aligned}
\tag{7}
$$

Table 1: Nomenclature

Variables (see Figure 1(a))	
α	Pitch angle (Positive counterclockwise)
h	Plunging displacement (Positive downwards)
β	Flap angle (Positive counterclockwise)
Aerodynamic Forces/Torques (see Figure 1(b))	
L	Resultant aerodynamic force at point 1
M_α	Torque due to L about point 3
M_β	Torque due to L about point 6
Structural Constants	
b	Half-chord of airfoil
m	Airfoil mass per unit length
I_i	Moments of inertia, $i = \{\alpha, \beta\}$
S_i	Static moments, $i = \{\alpha, \beta\}$
k_i	Elastic constraint stiffness, $i = \{\alpha, \beta, h\}$ (see Figure 1(b))
Geometrical Constants (Non-dimensional)	
a	Coordinate of axis of rotation (elastic center)
c	Coordinate of flap hinge
x_α	Distance of airfoil-flap mass center from a
x_χ	Distance of airfoil mass center from a
x_β	Distance of flap mass center from c

The moment of inertia of the entire airfoil I_α, the moment of inertia of the flap I_β, and the corresponding static moments $S_j, j = \{\alpha, \beta\}$ in the above expressions are measured with respect to the respective reference points (point 3 for the airfoil and point 6 for the flap, see Figure 1(b)). The

Lagrangian function in terms of the potential and kinetic energy expressions from (2) and (6), with the structural quantities as defined in (7) is given by,

$$
\mathcal{L} = \left\{ \frac{1}{2} I_\alpha \dot{\alpha}^2 + \frac{1}{2} I_\beta \dot{\beta}^2 + \frac{1}{2} m \dot{h}^2 + [I_\beta + b(c-a) S_\beta] \dot{\alpha}\dot{\beta} + S_\alpha \dot{h}\dot{\alpha} + S_\beta \dot{\beta}\dot{h} \right\}
$$
$$
- \frac{1}{2} \left\{ k_\alpha \alpha^2 + k_\beta \beta^2 + k_h h^2 \right\} \tag{8}
$$

The general expression for the non-conservative form of the Euler-Lagrange equations is [6],

$$
\frac{d}{dt} \left(\frac{\partial L}{\partial \dot{q}_i} \right) - \frac{\partial L}{\partial q_i} = Q_i, \quad i = 1, \dots, n \tag{9}
$$

For this particular problem we have $n = 3$ and $i = \alpha,\ \beta,\ h$. Let Q_i, $i = \{\alpha, \beta, h\}$ represent the generalized forces on the right hand side of the equation. The external forces on the airfoil arise due to the force $\vec{R}$ and the torque $\vec{M}_{ac}$ (see Figure 1(a)). The force R produces torques about reference points 3 and 6 which we shall call $\vec{M}_\alpha$, $\vec{M}_\beta$ using the notation of Theodorsen [2]. The generalized forces can then be obtained from a variational principle called the principle of virtual work (PVW) [6], which states that the external forces $\vec{Q}_i$ on a system produce no virtual work δW for virtual displacements $\delta \vec{q}_i$. The mathematical statement for the principle is

$$
\delta W = \sum_{i=1}^{n} \vec{Q}_i \cdot \delta \vec{q}_i = 0. \tag{10}
$$

The virtual displacements of a point on the airfoil can be written as $-\delta h \hat{\mathbf{i}}_2$, $-\delta \alpha \hat{\mathbf{i}}_3$ and $-\delta \beta \hat{\mathbf{i}}_3$ in the inertial frame I. Then the general statement of PVW from equation (10) gives,

$$
\begin{aligned}
\delta W &= \vec{R} \cdot (-\delta h \hat{\mathbf{i}}_2) + \vec{M}_\alpha \cdot (-\delta \alpha \hat{\mathbf{i}}_3) + \vec{M}_\beta \cdot (-\delta \beta \hat{\mathbf{i}}_3) = 0 \\
\Rightarrow \delta W &= L \hat{\mathbf{i}}_2 \cdot (-\delta h \hat{\mathbf{i}}_2) + (-M_\alpha \hat{\mathbf{i}}_3) \cdot (-\delta \alpha \hat{\mathbf{i}}_3) + (-M_\beta \hat{\mathbf{i}}_3) \cdot (-\delta \beta \hat{\mathbf{i}}_3) = 0 \\
\Rightarrow \delta W &= -L \delta h + M_\alpha \delta \alpha + M_\beta \delta \beta = 0
\end{aligned}
$$

9

which gives us the expressions for the generalized forces in terms of aerodynamic lift and torques,

$$Q_\alpha = M_\alpha, \quad Q_\beta = M_\beta \quad \text{and} \quad Q_h = -L \tag{11}$$

The Lagrangian (8) is substituted in equations (9) along with the relationships for the generalized forces from (11). Evaluating the expressions gives three 2nd order ordinary differential equations (ODE), which we reproduce from Theodorsen's paper [2],

$$
\begin{aligned}
I_\alpha \ddot{\alpha} + (I_\beta + b(c-a)S_\beta)\ddot{\beta} + S_\alpha \ddot{h} + k_\alpha \alpha &= M_\alpha \\
I_\beta \ddot{\beta} + (I_\beta + b(c-a)S_\beta)\ddot{\alpha} + S_\beta \ddot{h} + k_\beta \beta &= M_\beta \\
m\ddot{h} + S_\alpha \ddot{\alpha} + S_\beta \ddot{\beta} + k_h h &= -L
\end{aligned}
\tag{12}
$$

The left hand side of equations (12) gives the contributions from the structural dynamics of the airfoil. The right hand side terms representing the aerodynamic forces arise from the interaction of the airfoil with the surrounding flow. In the Theodorsen paper [2] the aerodynamic forcing terms on the right hand side were expressed as linear functions of $(\alpha, \beta, \dot{\alpha}, \dot{\beta}, \dot{h}, \ddot{\alpha}, \ddot{\beta}, \ddot{h})$. These functions arose from the aerodynamic model chosen by Theodorsen, which assumed a thin airfoil limited to small oscillations in an unsteady incompressible flow. We will first develop a simple incompressible and irrotational steady state aerodynamic model in the next section for a thin airfoil undergoing small amplitude oscillations. This introduces a basic steady linear model for our system. We will at first not include any nonlinearities and assume constant stiffness coefficients k_i in the equations (12). The generalized forces L, M_α, and M_β will be linear functions of α, β and h (see section 5).

10

Following this development, we will incorporate more sophisticated unsteady aerodynamics with the generalized functions expressed as linear functions of the generalized coordinates and their time derivatives (see section 7). Finally, nonlinearities will be introduced in the unsteady model by replacing the stiffness coefficients with polynomial stiffness terms.

4   Steady Aerodynamic Model

The terms on the right hand side of equations (12) represent the restoring aerodynamic force and torques on the airfoil. We want to develop an aerodynamic model for these forces that can be expressed only as a linear combination of the generalized coordinates α, β, and h. As an airfoil moves through the air, there is surrounding pressure distribution, which can be integrated over the airfoil surface to give a single resultant force R and a torque M_{ac} acting at the aerodynamic center (point 1 in Figure 1(a)).
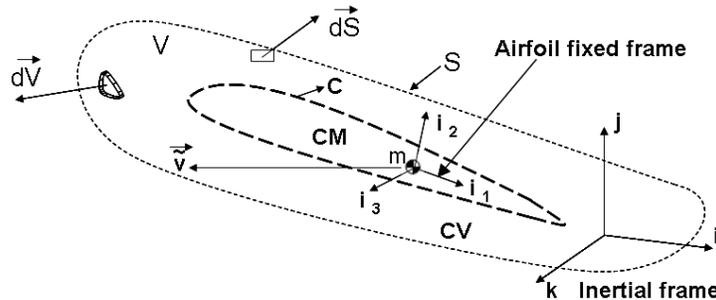
Figure 2: Airfoil control mass (CM) within a control volume (CV) with an integration contour C defined. Also shown are the inertial (Eulerian) and airfoil fixed (Lagrangian) reference frames.

Consider an airfoil control mass (CM) enclosed in a control volume (CV) V, with control surface S in an inertial reference frame (i, j, k) (see Figure 2).

The airfoil CM is attached to an airfoil-fixed right handed Cartesian reference frame $(\hat{i}_1, \hat{i}_2, \hat{i}_3)$ moving in time t. The airfoil CM has constant mass m and velocity $\vec{\tilde{v}} = \vec{\tilde{v}}(t)$. The flow field enclosed in the CV around the airfoil is variable with both space and time. Its density is $\rho_\infty = \rho_\infty(\vec{x}, t)$ and velocity is $\vec{v} = v_x(\vec{x}, t)\,\hat{i} + v_y(\vec{x}, t)\,\hat{j} + v_z(\vec{x}, t)\,\hat{k}$, defined in the inertial reference frame. The airfoil has a pressure distribution $p = p(\vec{x}, t)$ due to the flow field. We wish to relate the temporal dynamics of the airfoil CM viewed from a Lagrangian frame (moving with the airfoil) to the properties of the CV viewed from a fixed Eulerian frame of reference. Reynolds' Transport Theorem (RTT) is a general conservation law that relates CM conservation laws to the CV under consideration [7]. It states that for a general continuum property $\Psi = \Psi(\vec{x}, t)$ with a corresponding mass dependent property $\psi = \psi(\vec{x}, t) = \frac{\partial \Psi}{\partial m}$,

$$\frac{d}{dt} \iiint_{CM} \Psi \, dV = \frac{d}{dt} \iiint_V \rho\psi \, dV + \iint_S \rho\psi \, (\vec{v} \cdot d\vec{S}) \qquad (13)$$

To write mass conservation equations, we consider mass as the property of interest, letting $\Psi = m$ so that $\psi = 1$. Substituting this in equation (13),

$$\frac{d}{dt} \iiint_{CM} m \, dV = \frac{d}{dt} \iiint_V \rho \, dV + \iint_S \rho \, (\vec{v} \cdot d\vec{S})$$

The left hand side of the above equation represents the time rate of change of density of the airfoil CM, which is invariant. The equation then leads to the general continuity equation of fluid mechanics [4],

$$\frac{d}{dt} \iiint_V \rho \, dV + \iint_S \rho \, (\vec{v} \cdot d\vec{S}) = 0 \qquad (14)$$

For momentum conservation laws, the continuum property of interest is momentum. We let $\Psi = m\vec{v}$ and correspondingly $\psi = \vec{v}$. Then, substituting

this in the RTT equation (13),

$$\frac{d}{dt} \iiint_{CM} m\vec{\tilde{v}} \, dV = \frac{d}{dt} \iiint_V \rho\vec{v} \, dV + \iint_S \rho\vec{v} \, (\vec{v} \cdot d\vec{S}) \qquad (15)$$

The left hand side of equation (15) Newton's 2nd Law (constant mass) relates the momentum of the airfoil CM to the force it experiences,

$$\vec{F} = m\frac{d}{dt}(\vec{\tilde{v}}) \qquad (16)$$

The force $\vec{F}$ on the airfoil CM is split into a volume force $\vec{f}$ acting on a unit elemental volume dV, a force due to viscous shear stresses, represented simply by $\vec{F}_v$ and a pressure force p acting on an elemental area dS. Then, for the control volume V and control surface S, equation (15) gives,

$$-\iint_S p \, d\vec{S} + \iiint_V \rho\vec{f} \, dV + \vec{F}_v = \frac{\partial}{\partial t} \iiint_V \rho\vec{v} \, dV + \iint_S (\rho\vec{v} \cdot d\vec{S}) \, \vec{v} \quad (17)$$

The continuity and momentum conservation equations do not have closed form solutions. Consequently, we impose certain conditions on the flow properties. First, the flow around the airfoil is assumed to be changing so slowly that a steady state in time can be assumed. Second, the flow is assumed to be incompressible (a good approximation [4] for a flow Mach number is $M \lesssim 0.3$) making $\rho = \rho_\infty$ a constant, where the subscript ∞ refers to freestream flow, far from the airfoil. Then, with these assumptions and applying the divergence theorem to the continuity equation (14),

$$\rho_\infty \iint_S (\vec{v} \cdot d\vec{S}) \;=\; \rho_\infty \iiint_V (\vec{\nabla} \cdot \vec{v}) \, dV = 0$$

$$\Rightarrow \quad \vec{\nabla} \cdot \vec{v} = 0 \qquad (18)$$

The third assumption is of irrotational flow, which implies that $\vec{\nabla} \times \vec{v} = 0$. This allows us to define a potential flow such that the velocity of the flow

at every point is the gradient of a scalar potential function $\phi(x, y, z)$:

$$\vec{\nabla} \times \vec{v} = 0 \Leftrightarrow \vec{v} = \vec{\nabla}\phi(x, y, z). \tag{19}$$

Immediately, from equations (18, 19) we obtain Laplace's equation [4], governing incompressible, irrotational flow.

$$\nabla^2 \phi = 0 \tag{20}$$

Because the equation is linear, a complicated flow about an airfoil can be broken into several elementary potential flows that are solutions to Laplace's equation. This is the basis for thin airfoil theory [8, 9] which we shall use later. There are two boundary conditions [4] associated with equation (20) for the case of flow over a solid body. The first assumes that perturbations go to zero far from the body. Thus, we can define the freestream flow conditions as being *uniform* [4] i.e. $\vec{v} = v_\infty \hat{i}$. The second is the flow tangency condition for a solid body, which states that its physically impossible for a flow to cross the solid body boundary i.e. $\vec{\nabla}\phi \cdot \hat{n} = 0$.

Now we take a look at the momentum conservation equation (17). The irrotationality and incompressibility criteria imply that the flow is inviscid; i.e., friction, thermal conduction, and diffusion effects are not present (these effects are negligible for high Reynolds numbers associated with aircraft flight [4]). We have already neglected inertial forces in our derivation of the Euler-Lagrange equations so that, $\vec{f} = 0$. For 2D airfoils, with unit depth in the $\hat{k}$ direction and the integration contour C defined as shown in Figure 2, equation (17) then reduces to:

$$-\oint_C p\,\vec{dS} = \rho_\infty v_\infty \oint_C (\vec{v_\infty} \cdot \vec{dS}) \tag{21}$$

The left hand side represents the force R due to the pressure distribution on the airfoil. An expression for this can be calculated from either of the two

14

integrals in equation (21). However, since we have assumed incompressible, irrotational flow, we can take advantage of the Kutta-Juokowski Theorem [4] that relates the force (R) experienced by a two dimensional body of arbitrary (with some smoothness limitations) cross sectional area immersed in an incompressible, irrotational flow to the magnitude of the circulation Γ around the body. Mathematically the Kutta-Juokowski Theorem states,

$$\vec{R} = \rho_\infty \vec{v_\infty} \times \vec{\Gamma}, \quad \text{where} \quad \vec{\Gamma} = -\oint_C (\vec{v} \cdot d\vec{S}) \tag{22}$$

Before moving onto thin airfoil theory [8, 9], a brief discussion of the inviscid flow assumption is in order. The condition of inviscid flow follows directly from the condition of irrotationality as a consequence of Kelvin's Circulation Theorem [4], which proves that for an inviscid flow, with conservative body forces (in our case, body forces are zero), the circulation remains constant along a closed contour. This implies that there is no change in the vorticity, $\vec{\nabla} \times \vec{v}$, with time:

$$\frac{d\Gamma}{dt} = -\frac{d}{dt} \oint_C (\vec{v} \cdot d\vec{S}) = -\frac{d}{dt} \iint_S (\vec{\nabla} \times \vec{v}) \cdot d\vec{S} = 0 \tag{23}$$

If the vorticity is zero in the absence of inviscid forces (as is the case for irrotational flow), the flow remains irrotational. The major drawback of ignoring viscosity is that zero drag is predicted for the airfoil ("d'Alembert's paradox" [4]), which we can see using equation (22). The lift force L is defined as normal to the free stream whereas the drag force D is always parallel to the flow (See Figure 1(a)). Taking force components normal and parallel to the freestream flow yields,

$$
\begin{aligned}
L &= \rho_\infty \, |\vec{v_\infty}| \, |\vec{\Gamma}| \, \sin(\frac{\pi}{2}) = \rho_\infty v_\infty \Gamma \\
D &= \rho_\infty \, |\vec{v_\infty}| \, |\vec{\Gamma}| \, \sin(0) = 0
\end{aligned}
\tag{24}
$$

15

This paradox is resolved with the justification that the drag force is always parallel to the translational DOF for the airfoil h and can thus be safely ignored in our equations of motion. The drag force vector rotates about the mean chord line, but as we are assuming small oscillations, any torques that could affect the two rotational DOF α and β are neglected.

5   Steady Thin Airfoil Aerodynamic Theory

Classical thin airfoil theory assumes that the flow around an airfoil can be described by the superposition of two potential flows, such that the entire flow around the airfoil has a velocity potential function that is a solution to Laplace's equation (20). The first potential flow is a uniform freestream flow that we have already described, $\vec{v} = v_\infty \hat{i}$. To this is added a second component of velocity, induced by the presence of the airfoil in the moving flow.

The fundamental assumption of the theory is that the velocity induced by the airfoil is equivalent to the sum of induced velocities of a line of elemental vortices, called a vortex sheet, placed on the chord line of the airfoil (see Figure 3). Thus, the airfoil itself can be replaced by the vortex sheet in the model. In reality, there is a thin layer of high vorticity on the surface of an airfoil due to viscous effects. Our model is justified if one includes the restriction that the airfoil be thin enough to model with just the chord line. The NACA standard definition for a thin airfoil is that the thickness is no greater than 10% of the chord i.e. $t_{max} \leq 0.1(2b)$, where t_{max} is the maximum airfoil thickness and b is the half chord [5].

Replacing the airfoil with an equivalent vortex sheet on the mean chord line (Figure 3) produces a velocity distribution consistent with vortex flow,
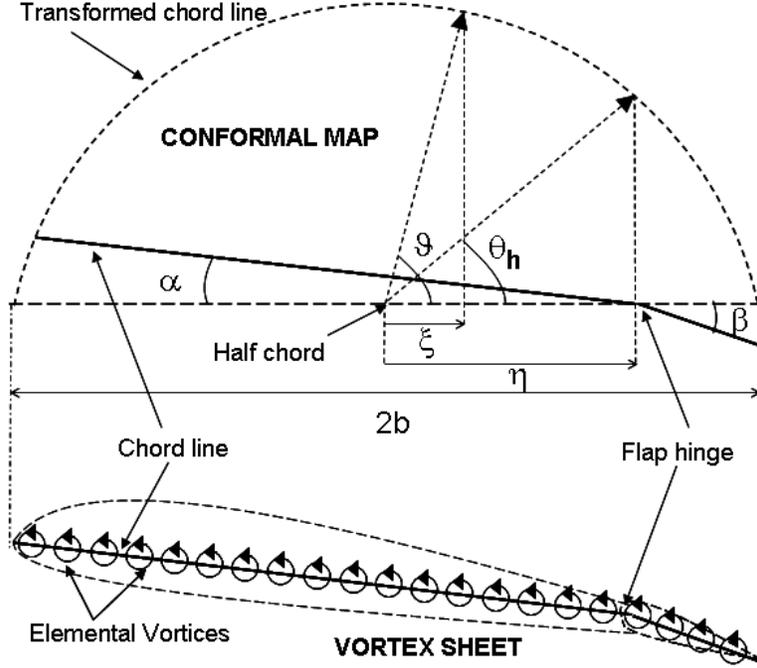
Figure 3: The airfoil (shown at the bottom) is replaced with a vortex sheet along its chord line. The chord line (shown on top) is then transformed to a half circle by the conformal map $\xi = b(1 - \cos(\vartheta))$. The flap location η is mapped to an angle θ_h.

which is a potential flow and hence satisfies Laplace's equation (20). The strength of each elemental vortex located at a distance x is $\gamma = \gamma(x)$. The circulation around the airfoil arises from the contribution of all the elemental vortices:

$$\Gamma = \int_0^{2b} \gamma(\xi)\, d\xi \tag{25}$$

The mean chord line of the airfoil is transformed via a conformal map such that the airfoil coordinate ξ (see Figure 3) is replaced by an angle ϑ [8]. The flap hinge coordinate η is transformed to the angle θ_h. The conformal

17

map is given by the equation:

$$\xi = b(1 - \cos(\vartheta)) \tag{26}$$

where the flap hinge location in Figure 3 is given by $\eta = b(1 - \cos(\theta_h))$.

The lift per unit span, $L = \rho_\infty v_\infty \Gamma$ is obtained using the Kutta-Joukowski Theorem (22). At this point, it is convenient to introduce a dimensionless variable known as the section lift coefficient [4], defined as,

$$c_l = \frac{L}{\frac{1}{2}\rho_\infty v_\infty^2 (2b)} = \frac{L}{b\rho_\infty v_\infty^2} = \frac{\Gamma}{b v_\infty} \tag{27}$$

where b is the half chord length from Figure 1(b). From dimensional analysis [4], in general for a given flow $c_l = c_l(\alpha, \beta)$. Expanding this with a first order Taylor approximation,

$$c_l = c_l(0,0) + \frac{\partial c_l(0,0)}{\partial \alpha}\alpha + \frac{\partial c_l(0,0)}{\partial \beta}\beta \tag{28}$$

Thin airfoil theory [8] gives constant expressions for the partial derivatives in equation (28). We are assuming a symmetric airfoil, which makes $c_l(0,0) = 0$ [4]. Then,

$$c_l = 2\pi\,\alpha + 2[(\pi - \theta_h) + \sin(\theta_h)]\,\beta$$

Noting from Figure 1(b) and Figure 3 that the length of the flap chord is $b(1 - c) = b - \eta$ and using the inverse of the conformal map defined in equation (26),

$$c_l = \sigma_1\,\alpha + \sigma_2\,\beta \tag{29}$$

where σ_1, σ_2 are constants (see the Appendix).

The aerodynamic torque about an arbitrary point x_0 on the airfoil can be expressed in terms of the strength γ of each elemental vortex as,

$$M = -\rho_\infty v_\infty \int_0^{2b} (\xi - x_0)\,\gamma(\xi - x_0)\,d\xi$$

18

We are interested in the aerodynamic torque M_α about the elastic center (point 3 in Figure 1(b)) that appears in equation (12). However, thin airfoil theory provides results [8] for the aerodynamic torque M_{ac} about the aerodynamic center, which is coincident with the quarter chord point (point 1 in Figure 1(b)) for a thin airfoil [4]. We proceed by deriving an expression relating M_α to M_{ac}. Summing torques about point 3 in Figure 1(b),

$$\vec{M}_\alpha = \vec{M}_{ac} + \vec{r}_{13} \times \vec{L} \tag{30}$$

where, $\vec{r}_{13}$ is the vector from point 1 to 3 and the lift vector $\vec{L}$ is always orthogonal to the chord line and hence to $\vec{r}_{13}$. Also, from Figure 1(b), $|\vec{r}_{13}| = b\left(\frac{1}{2} + a\right)$.

Analogous to the section lift coefficient is the section moment coefficient [4],

$$c_m = \frac{M}{\frac{1}{2}(2b)^2 \rho_\infty v_\infty^2} = \frac{M}{2b^2 \rho_\infty v_\infty^2} \tag{31}$$

Expressing the torques in equation (30) in terms of moment coefficients (31) and the lift coefficient defined in equation (27),

$$c_{m,\alpha} = c_{m,ac} + \frac{c_l}{2}\left(a + \frac{1}{2}\right) \tag{32}$$

As before, $c_{m,ac} = c_{m,ac}(\alpha, \beta)$ [4]. Expanding this with a first order Taylor approximation,

$$c_{m,ac}(\alpha, \beta) = c_{m,ac}(0,0) + \frac{\partial c_{m,ac}(0,0)}{\partial \alpha}\alpha + \frac{\partial c_{m,ac}(0,0)}{\partial \beta}\beta \tag{33}$$

The aerodynamic center is a convenient reference because the aerodynamic torque about this point is independent of the angle of attack [4] which implies $\frac{\partial c_{m,ac}}{\partial \alpha} = 0$ and for a symmetric airfoil, $c_{m,ac}(0,0) = 0$ [4]. Thin airfoil theory gives constant values [8] (see σ_3, σ_4 in the Appendix) for the partial

19

derivatives in equation (33) which are substituted back into equation(32) along with the expression for c_l from equation (29) to obtain,

$$c_{m,\alpha} = \sigma_5\,\alpha + \sigma_6\,\beta \qquad (34)$$

where the constant terms σ_5, σ_6 are given in the Appendix.

The hinge torque M_β about the flap hinge (point 6 in Figure 1(b)) arises due to the pressure distribution on the flap. The hinge torque about an arbitrary point $\tilde{x}_0$ on the flap can be expressed in terms of the strength γ of the elemental vortices arranged along the flap chord,

$$M_\beta = -\rho_\infty v_\infty \int_{bc}^{b} (\xi - \tilde{x}_0)\,\gamma(\xi - \tilde{x}_0)\,d\eta$$

As before, a section hinge moment coefficient is defined with the airfoil chord b replaced by the flap chord $b(1-c)$ (see Figure 1(b)),

$$c_{m,\beta} = c_{m,\beta}(\alpha,\beta) = \frac{M_\beta}{\frac{1}{2}(b(1-c))^2\rho_\infty v_\infty^2} \qquad (35)$$

From the results of thin airfoil theory [9] we directly obtain constants for the partial derivatives in the first order Taylor expansion (see the Appendix),

$$c_{m,\beta}(\alpha,\beta) = c_{m,\beta}(0,0) + \frac{\partial c_{m,\beta}(0,0)}{\partial\alpha}\alpha + \frac{\partial c_{m,\beta}(0,0)}{\partial\beta}\beta = \sigma_7\alpha + \sigma_8\beta \quad (36)$$

Finally, the aerodynamic force and torque expressions from equations $(27, 31)$ can be written in terms of the defined constants (see equations (50) in the Appendix) as linear functions of α and β,

$$
\begin{aligned}
L &= b\rho_\infty v_\infty^2(\sigma_1\alpha + \sigma_2\beta) \\
M_\alpha &= 2b^2\rho_\infty v_\infty^2(\sigma_5\alpha + \sigma_6\beta) \qquad (37) \\
M_\beta &= \frac{1}{2}b^2(1-c)^2\rho_\infty v_\infty^2(\sigma_7\alpha + \sigma_8\beta)
\end{aligned}
$$

6 Steady Linear Aeroelastic Model

We combine the aeroelastic equations of motion developed in section 3 with the linear steady aerodynamics developed in section 5 to obtain an aeroelastic model for the system. The main limitation is an assumption of steadiness of the flow around the airfoil with respect to time. Combining equations (12) and (37), we write the model equations of motion in matrix form.

$$
\begin{bmatrix}
I_\alpha & (I_\beta + b(c-a)S_\beta) & S_\alpha \\
(I_\beta + b(c-a)S_\beta) & I_\beta & S_\beta \\
S_\alpha & S_\beta & m
\end{bmatrix}
\begin{Bmatrix} \ddot{\alpha} \\ \ddot{\beta} \\ \ddot{h} \end{Bmatrix} +
$$

$$
\begin{bmatrix}
k_\alpha - 2b^2\rho_\infty v_\infty^2 \sigma_5 & -2b^2\rho_\infty v_\infty^2 \sigma_6 & 0 \\
-\frac{1}{2}b^2(1-c)^2\rho_\infty v_\infty^2 \sigma_7 & k_\beta - \frac{1}{2}b^2(1-c)^2\rho_\infty v_\infty^2 \sigma_7 & 0 \\
b\rho_\infty v_\infty^2 \sigma_1 & b\rho_\infty v_\infty^2 \sigma_2 & k_h
\end{bmatrix}
\begin{Bmatrix} \alpha \\ \beta \\ h \end{Bmatrix} =
\begin{Bmatrix} 0 \\ 0 \\ 0 \end{Bmatrix}
\tag{38}
$$

Note that the equations are of the general form $[M]\ddot{\vec{q}} + [C]\dot{\vec{q}} + [K]\vec{q}$, where $\vec{q}$ is a vector of the system variables, $[M]$ is a symmetric inertia matrix, $[K]$ is a stiffness matrix with contributions from the strain energy of the system, the potential energy of the elastic constraints and the aerodynamic loads. The matrix $[C]$ represents the damping present in the system, and is null in this case because of the absence of any dissipative forces in this model. We rewrite the equations in first order form by introducing a change of variables $\{x_1, x_2, x_3, x_4, x_5, x_6\} = \{\alpha, \beta, h, \dot{\alpha}, \dot{\beta}, \dot{h}\}$ to obtain the following equation, where the constants a_i, $i = 1, 2 \ldots, 6$ and b_j, $j = 1, 2 \ldots, 9$ are expressions of the system constants from Table 1. This linear, 1st order ODE system has solutions of the form $\vec{x}(t) = \vec{\nu}_i e^{\lambda_i t}$, $i = \{1 \ldots 6\}$, where λ_i is an eigenvalue of the system given above with an associated eigenvector $\vec{\nu}_i$. The velocity v_∞ is shown explicitly in the matrix because of its importance

in this analysis.

$$
\left\{
\begin{array}{c}
\dot{x_1} \\
\dot{x_2} \\
\dot{x_3} \\
\dot{x_4} \\
\dot{x_5} \\
\dot{x_6}
\end{array}
\right\}
=
\left[
\begin{array}{cccccc}
0 & 0 & 0 & 1 & 0 & 0 \\
0 & 0 & 0 & 0 & 1 & 0 \\
0 & 0 & 0 & 0 & 0 & 1 \\
a_1 v_\infty^2 + b_1 & a_2 v_\infty^2 + b_2 & b_3 & 0 & 0 & 0 \\
a_3 v_\infty^2 + b_4 & a_4 v_\infty^2 + b_5 & b_6 & 0 & 0 & 0 \\
a_5 v_\infty^2 + b_7 & a_6 v_\infty^2 + b_8 & b_9 & 0 & 0 & 0
\end{array}
\right]
\left\{
\begin{array}{c}
x_1 \\
x_2 \\
x_3 \\
x_4 \\
x_5 \\
x_6
\end{array}
\right\}
\tag{39}
$$

Prediction and characterization of the flutter boundary is our ultimate goal and the system behavior is studied for various values of v_∞. Numerical values for a real airfoil geometry with corresponding physical structural data, obtained from experimental results published in reference [10], are tabulated in Table 2. These numbers were used to numerically integrate the ODEs in equation (39) using a 4th order Runge-Kutta scheme with a 5th order correction. The airflow density was taken to be that at mean sea level. The numerics correspond to a physical situation where an airfoil is flown at sea level between speeds of 0 to $100\,m/s$. The limitations on the speed are a direct consequence of the incompressible, inviscid assumptions made in the aerodynamic model (see section 4), which only hold for a Mach number $M \lessgtr 0.3$, corresponding to an airflow velocity of $v_\infty \approx 100 m/s$. The airfoil was chosen to run at sea level because of this speed limitation in order to reflect a real physical regime in which aircraft operate - the takeoff roll. This usually occurs at speeds within the limits of our model at sea level. Speeds at the high end of this range are also normal for the initial ascent of small, low speed private commuter aircraft like the Cessna series of single engine turboprops [11].

Table 2: Physical Data

Structural Constants	
b	0.127 m
m	1.567 kg
I_α	0.01347 $kg\,m^2$
I_β	0.0003264 $kg\,m^2$
S_α	0.08587 $kg\,m$
S_β	0.00395 $kg\,m$
k_α	37.3 $kg\,m/s^2$
k_β	39 $kg\,m/s^2$
k_h	2818.8 $kg\,m/s^2$
ρ_∞	1.225 kg/m^3
Geometrical Constants (Non-dimensional)	
a	-0.5
c	0.5

The six eigenvalues of the system take the form $\Gamma_k \pm i\Omega_k$, $k = 1, 2, 3$, where the stability of the system is determined by the real part of the eigenvalues, Γ_k. The stability of the system is ensured if all $\Gamma_k \leq 0$. The system exhibits oscillatory behavior for non-zero values of the imaginary part Ω_k. The response for the set of parameters given in Table 2 is unstable over a significant range of velocities within the limit of the model, with divergent oscillations. The behavior of the imaginary part of the eigenvalues with changes in airflow speed is shown in Figure 4(b). A plot of Γ_k versus v_∞ from Figure 4(a), shows that the first bifurcation occurs at a value of $v_\infty \approx 25\,m/s$, where Γ_k first take a positive value. This bifurcation corre-
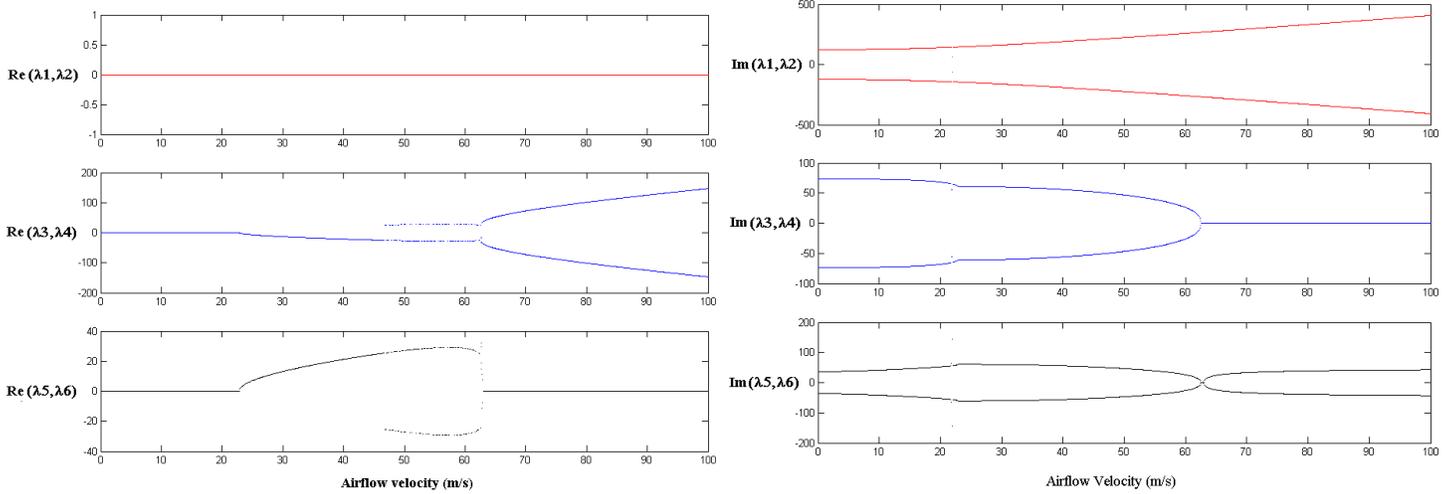
Figure 4: (a) Real part of eigenvalues plotted versus flow speed (in m/s). Note the first bifurcation for $v_\infty \approx 25\,m/s$. This is the predicted flutter velocity. (b)Imaginary part of eigenvalues plotted versus flow speed (in m/s). See Table 2 for values of system constants. The system dynamics for this configuration are divergent oscillations.

sponds to a change in the stability of the system from stable to divergent oscillations and is the predicted flutter boundary. The onset of flutter at such an early stage in the flight regime is highly undesirable because most modern aircraft take off at speeds $\sim 60\,m/s$ [11]. We seek to tailor the design of the airfoil such that flutter is delayed as long as possible. Within the limits of the present model, a flutter speed above $100\,m/s$ would be a good design objective because beyond this speed the model will no longer produce meaningful results.

With this design goal in mind, the behavior of the system was studied for changes in various model parameters. The first approach adopted was in varying the geometrical configuration of the airfoil. The location of the

24
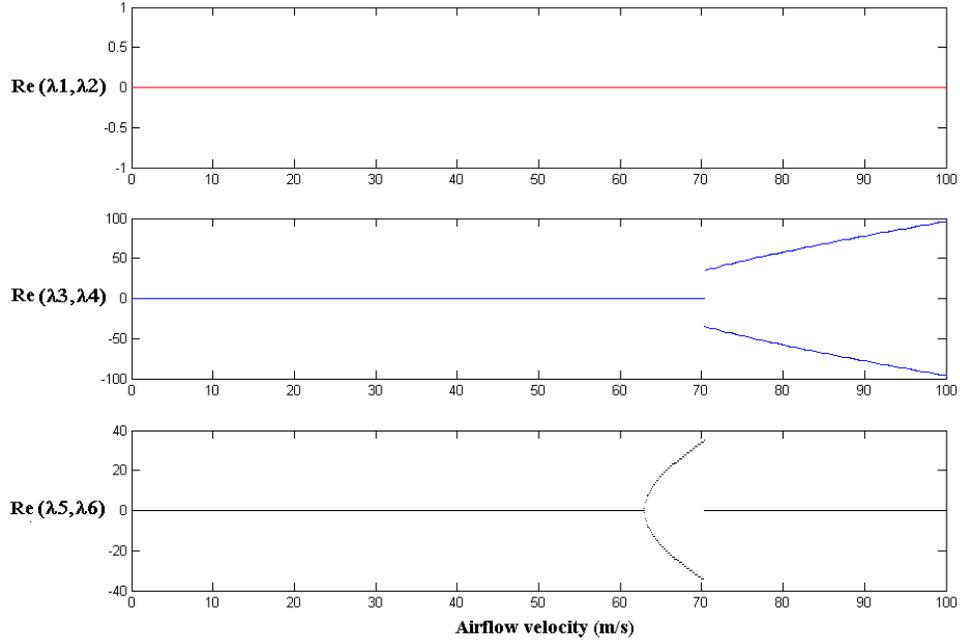
Figure 5: Real part of eigenvalues plotted versus flow speed (in m/s). $S_\alpha = 0.008587\,kg\,m$. Note the delayed first bifurcation for $v_\infty \approx 65\,m/s$, when compared to Figure 4. However, flutter is still predicted before the model limit of $v_\infty \approx 100\,m/s$

elastic center (point 3 in Figure 1(b)), corresponding to the value of a in Table 2 had no significant effect on the location of the first bifurcation point. The location of the airfoil CG (point 5 in Figure 1(b)) with respect to the elastic center was then changed. This corresponds to an increase or decrease in the static moment S_α (see Table 1 and equation (7) for definitions). Increasing S_α, which implies moving the center of gravity towards the TE of the airfoil, only worsened the situation with flutter occurring at even lower speeds. A decrease in S_α, obtained by moving the CG towards the LE of the airfoil did delay the onset of the first bifurcation. However, the flutter
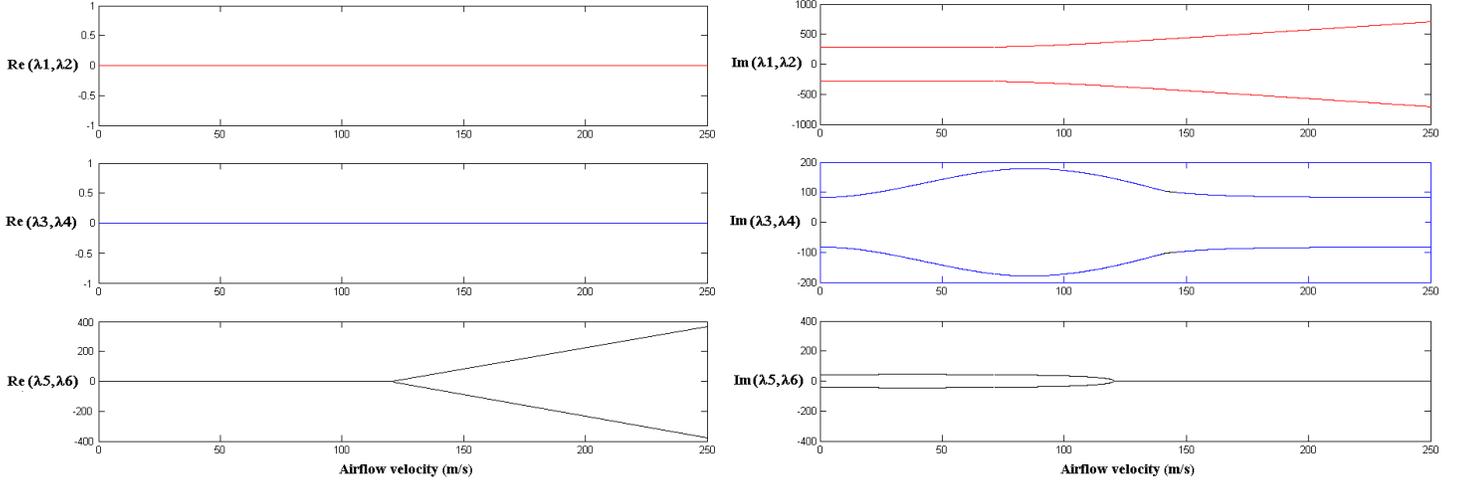
Figure 6: (a) Real part of eigenvalues plotted versus flow speed (in m/s). (b) Imaginary part of eigenvalues plotted versus flow speed (in m/s). $S_\alpha = 0.008587\,kg\,m$, $k_\alpha = 93.25\,kg\,m/s^2$, $k_\beta = 97.5\,kg\,m/s^2$. The airfoil stiffness has been increased by 250% and the CG is shifted forward towards the LE by 90%. Note the first bifurcation for $v_\infty \approx 125\,m/s$ falls outside the boundaries of the model ($v_\infty \lessapprox 100\,m/s$).

boundary was still within $100\,m/s$ for the maximum decrease in S_α possible physically. For example, the flutter boundary was pushed forward to around $70\,m/s$ for 10% of the original S_α (see Figure 5).

The second configuration change was altering the structural characteristics of the airfoil. The stiffness of the airfoil constraints in pitch, plunge and flap were changed. This approach successfully pushed the flutter boundary outside the physical envelope of this model. Combining a change in the geometry of the airfoil with a change in its structural stiffness produced the best results for the smallest alteration in the airfoil configuration. For example, a 250% increase in k_α and k_β (changing the stiffness of the air-

26
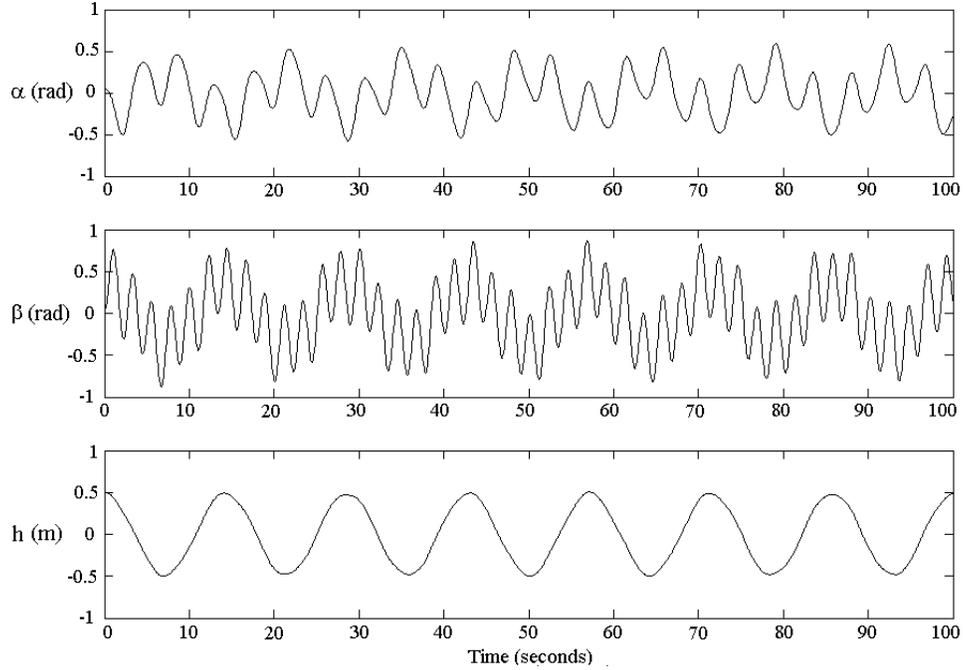
Figure 7: System dynamics for a simulation time of 100 seconds. $S_\alpha = 0.008587 \, kg \, m$, $k_\alpha = 93.25 \, kg \, m/s^2$, $k_\beta = 97.5 \, kg \, m/s^2$. Note that the oscillations do not diverge. The maximum deflection of the airfoil is about 0.5 m, which is twice the airfoil length. The pitch and flap oscillations are also within 1 radian.

foil in pitch and flap), combined with a 50% decrease in S_α produced the first bifurcation at a speed of around $120 \, m/s$. The bifurcation diagrams are shown in Figures 6(a) and (b). The stable oscillatory behavior of the system for the new parameters is shown in Figure 7.

The above analysis is deficient because of the shortcomings of our aerodynamic model. While the linear nature of the aerodynamics is one major limiting assumption, the major obstacle to obtaining a realistic picture of the dynamics is due to the absence of dissipative forces. The flow around

27

the airfoil changes with time and thus physically accurate predictions of flutter speed can only be made using unsteady aerodynamics [1]. However, at least some qualitative inferences can be made from this limited model. The flutter speed dependence on the system parameters has been established. It is also evidently possible to delay the onset of instability by changing the structure of the airfoil. For example, moving the CG location of the airfoil forward with respect to its elastic axis, towards the LE, while stiffening the airfoil structurally leads to an increase in the flutter speed for the linear aerodynamic model.

7 Incorporating Dissipation in the Model

In previous sections, we have seen the limitations of the steady state aerodynamic model, where the generalized aerodynamic force and torques were linear scleronomic constraints of the form $Q_i = f(\vec{q})$, $i = \alpha, \beta, h$, where $\vec{q}$ is a vector of the generalized coordinates. A steady state model predicts unrealistic flutter boundaries because the steadiness assumption neglects perturbations that arise due to airfoil-flow interactions. The surrounding air exerts frictional forces that would tend to retard the motion of the airfoil. For systems where the amplitude of oscillations is small compared to the magnitude of the dissipation, the generalized damping constraint forces are linear functions of the form $Q_{fr,i} = f(\dot{\vec{q}}) = -\sum_i c_{ij}\dot{q}_i$. It is possible to write this in terms of a dissipative function, $F_{fr} = \frac{1}{2}\sum_{i,j} c_{ij}\dot{q}_i\dot{q}_j$ where $c_{ij} = c_{ji}$, such that $Q_{fr,i} = -\frac{\partial F_{fr}}{\partial \dot{q}_i}$. We add this dissipative function to the right hand side of Lagrange's equations (9) to obtain the following equations [12],

$$\frac{d}{dt}\left(\frac{\partial L}{\partial \dot{q}_i}\right) - \frac{\partial L}{\partial q_i} = Q_i - \frac{\partial F_{fr}}{\partial \dot{q}_i}, \quad i = 1, 2, 3 \tag{40}$$

We need expressions for the generalized forces on the right hand side of the above equation. Deriving a dissipative aerodynamic model from first principles is beyond the scope of this paper. Instead, we adopt an unsteady model developed by Theodorsen for a thin airfoil oscillating in an incompressible flow [2]. In this model, the sources of dissipation in the airfoil-flow system are classified according to two distinct physical phenomena - circulatory and non-circulatory effects [1]. To understand the origin of circulatory effects, we recall Kelvin's circulation theorem discussed in section 4, which states that the circulation remains constant along a closed contour for an inviscid flow (neglecting inertial forces). This implies that the vortices developed on the airfoil surface (see Figure 3) shed vortices of equal strength and opposite rotation in the surrounding flow in order to produce no change in the overall circulation. These counter-rotating vortices would produce an induced flow that would effectively change the flow field around the airfoil. As the airfoil moves, a succession of these vortices would be continuously formed leading to unsteady flow around the airfoil dependent on the strength and distance of these vortices.

Non-circulatory effects arise due to the inertia of the mass of air surrounding the airfoil, which we have neglected so far. A perturbation to the airfoil that produces a net acceleration would be opposed by the inertial force of this mass of air. So, the total contribution to the generalized forces on the right hand side of equations (40) comes from scleronomic constraints, inertial constraints and frictional damping. According to Theodorsen's model, the aerodynamic force L and torques M_α, M_β can be expressed as linear functions of $\{\alpha, \dot{\alpha}, \ddot{\alpha}, \beta, \dot{\beta}, \ddot{\beta}, \dot{h}, \ddot{h}\}$ (the coefficient of h is zero) as follows:

$$
\begin{aligned}
L = \; & - \; \rho_\infty b^2 \left[-\pi a b \ddot{\alpha} - T_1 b \ddot{\beta} + \pi \ddot{h} + \pi v_\infty \dot{\alpha} - T_4 v_\infty \dot{\beta} \right] \\
& - \; 2\pi \rho_\infty b v_\infty C(k) \left[b \left(\frac{1}{2} - a \right) \dot{\alpha} + \frac{T_{11}}{2\pi} b \dot{\beta} + \dot{h} + v_\infty \alpha + \frac{T_{10}}{\pi} v_\infty \beta \right]
\end{aligned}
$$

$$
\begin{aligned}
M_\alpha = \; & - \; \rho_\infty b^2 \left[\pi b^2 \left(\frac{1}{8} + a^2 \right) \ddot{\alpha} - \left(T_7 + (c-a)T_1 \right) b^2 \ddot{\beta} - \pi a b \ddot{h} \right] \\
& - \; \rho_\infty b^2 \left[\left(\frac{1}{2} - a \right) \pi b v_\infty \dot{\alpha} + \left(T_1 - T_8 - (c-a)T_4 + \frac{1}{2} T_{11} \right) b v_\infty \dot{\beta} + (T_4 + T_{10}) v_\infty^2 \beta \right] \\
& + \; 2\pi \rho_\infty \left(a + \frac{1}{2} \right) b^2 v_\infty C(k) \left[b \left(\frac{1}{2} - a \right) \dot{\alpha} + \frac{T_{11}}{2\pi} b \dot{\beta} + \dot{h} + v_\infty \alpha + \frac{T_{10}}{\pi} v_\infty \beta \right] \qquad (41)
\end{aligned}
$$

$$
\begin{aligned}
M_\beta = \; & - \; \rho_\infty b^2 \left[2 T_{13} b^2 \ddot{\alpha} - \frac{T_3}{\pi} b^2 \ddot{\beta} - T_1 b \ddot{h} \right] \\
& - \; \rho_\infty b^2 \left[\left\{ T_4 \left(a - \frac{1}{2} \right) - T_1 - 2 T_9 \right\} b v_\infty \dot{\alpha} - \frac{T_4 T_{11}}{2\pi} b v_\infty \dot{\beta} + \left(\frac{T_5 - T_4 T_{10}}{\pi} \right) v_\infty^2 \beta \right] \\
& - \; T_{12} \rho_\infty b^2 v_\infty C(k) \left[b \left(\frac{1}{2} - a \right) \dot{\alpha} + \frac{T_{11}}{2\pi} b \dot{\beta} + \dot{h} + v_\infty \alpha + \frac{T_{10}}{\pi} v_\infty \beta \right]
\end{aligned}
$$

Here, a, b are the usual airfoil geometrical constants defined in Figure 1, and Table 1 and ρ_∞, and v_∞ are the constant freestream density and velocity respectively. The constants T_i, $i = 1, 2, \ldots, 14$ arise from the velocity potentials [2] and can be expressed in terms of the airfoil constant c (see Figure 1), analogous to the constants for the steady model, σ_i (see equations(50) in the Appendix).

The contribution from the circulatory effects is contained in the last term in each of equations (41). The effect of the shed vortices is modeled using the function $C(k)$, where k, known as the reduced frequency, is a dimensionless parameter that is a measure of the extent of dissipation in the model. The reduced frequency can be expressed in terms of flow speed v_∞, airfoil half chord b and the natural frequency of the motion ω as $k = \frac{b\omega}{v_\infty}$. The Theodorsen function $C(k)$ is a complex valued function [2] that is given by, $C(k) = F(k) + iG(k)$, where $F(k)$ and $G(k)$ are Bessel functions.

The Theodorsen function introduces a phase lag between airfoil oscillations and resulting changes in the surrounding airflow. Its value also determines the magnitude of change in the lift force due to unsteady effects, which is the reason it is sometimes called the lift deficiency function. The terms in equations (41) that do not contain $C(k)$ arise from the non-circulatory effects of the potential flow. Their contribution to the overall force and torques is less significant than the circulatory term because inertial forces on an airfoil tend to be smaller than the pressure forces [1].

8 Linear Quasi-Steady Aeroelastic Model

We adopt an approximation of Theodorsen's theory by setting $C(k) = 1$ in equations (41). This neglects any lag between unsteady oscillations and their effect on aerodynamic force and torques, limiting us to oscillations that are changing slowly. Referring to Figure 4 in reference [2], which contains plots of the real and imaginary parts $F(k)$ and $G(k)$ of the Theodorsen function, we note that $k \lesssim 0.1$ for $C(k) = 1$. Apart from neglecting the phase lag, the forces produced by unsteady effects on the airfoil are assumed to be small compared to those arising due to steady effects. For this reason, such an approximation of Theodorsen's theory is known as "quasi-steady" thin airfoil theory [1].

We set $C(k) = 1$ in equations (41) and use them as expressions for the generalized forces on the right hand side in equations (12). This leads to linear second order equations of motion for a quasi-steady aeroelastic model, expressed in general matrix form as, $[M]\vec{\ddot{q}} + [C]\vec{\dot{q}} + [K]\vec{q} = \{0\}$, where $\vec{q} = \{\alpha, \beta, h\}$ is a vector of the system variables, $[M]$ is a symmetric inertia matrix, $[C]$ contains terms arising from the dissipation in the system

31

Table 3: Physical Data for Quasi-Steady Model

Nondimensional Constants	
x_α	0.2
x_β	0
r_α	0.5
r_β	0.035
ω_α	90
ω_β	22.5
ω_h	27.56
k	0.25
a	-0.5
c	0.6
Dimensional Constants (Non-dimensional)	
b	1.829 m
m	12.207 kg

and $[K]$ is a stiffness matrix with contributions from the strain energy of the system, the potential energy of the elastic constraints and the aerodynamic loads. Written explicitly,

$$
\begin{bmatrix}
I_\alpha + \pi\left(\frac{1}{8}+a^2\right)\rho_\infty b^4 & I_\beta + b(c-a)S_\beta + 2T_{13}\rho_\infty b^4 & S_\alpha - \pi\rho_\infty a b^3 \\
I_\beta + b(c-a)S_\beta + 2T_{13}\rho_\infty b^4 & I_\beta - \frac{T_3}{\pi}\rho_\infty b^4 & S_\beta - T_1\rho_\infty b^3 \\
S_\alpha - \pi\rho_\infty a b^3 & S_\beta - T_1\rho_\infty b^3 & m + \pi\rho_\infty b^2
\end{bmatrix}
\left\{\begin{array}{c}\ddot\alpha\\\ddot\beta\\\ddot h\end{array}\right\} +
$$

$$
\begin{bmatrix}
\left[\left(\frac{1}{2}-a\right)+2\left(a^2-\frac{1}{4}\right)C(k)\right]\pi\rho_\infty b^3 v_\infty & \left[T_1 - T_8 - (c-a)T_4 + \frac{1}{2}T_{11} - \left(a+\frac{1}{2}\right)T_{11}C(k)\right]\rho_\infty b^3 v_\infty & -2\pi\left(a+\frac{1}{2}\right)C(k)\rho_\infty b^2 v_\infty \\
\left[T_4\left(a-\frac{1}{2}\right)-T_1-2T_9+T_{12}\left(\frac{1}{2}-a\right)C(k)\right]\rho_\infty b^3 v_\infty & -\left[T_4 T_{11}-T_{11}T_{12}C(k)\right]\frac{\rho_\infty}{2\pi}b^3 v_\infty & T_{12}C(k)\rho_\infty b^2 v_\infty \\
\left[1+(1-2a)C(k)\right]\pi\rho_\infty b^2 v_\infty & -(T_4 - T_{11}C(k))\rho_\infty b^2 v_\infty & 2\pi C(k)\rho_\infty b v_\infty
\end{bmatrix}
\left\{\begin{array}{c}\dot\alpha\\\dot\beta\\\dot h\end{array}\right\}
$$

$$
+
\begin{bmatrix}
k_\alpha - 2\pi\left(a+\frac{1}{2}\right)C(k)\rho_\infty b^2 v_\infty^2 & \left[T_4 + T_{10} - 2\left(a+\frac{1}{2}\right)T_{10}C(k)\right]\rho_\infty b^2 v_\infty^2 & 0 \\
T_{12}C(k)\rho_\infty b^2 v_\infty^2 & k_\beta + (T_5 - T_4 T_{10} + T_{10}T_{12}C(k))\frac{\rho_\infty}{\pi}b^2 v_\infty^2 & 0 \\
2\pi C(k)\rho_\infty b v_\infty^2 & 2T_{10}C(k)\rho_\infty b v_\infty^2 & k_h
\end{bmatrix}
\left\{\begin{array}{c}\alpha\\\beta\\h\end{array}\right\} = \left\{\begin{array}{c}0\\0\\0\end{array}\right\} \qquad (42)
$$

At this point, it is convenient to introduce the following nondimension-
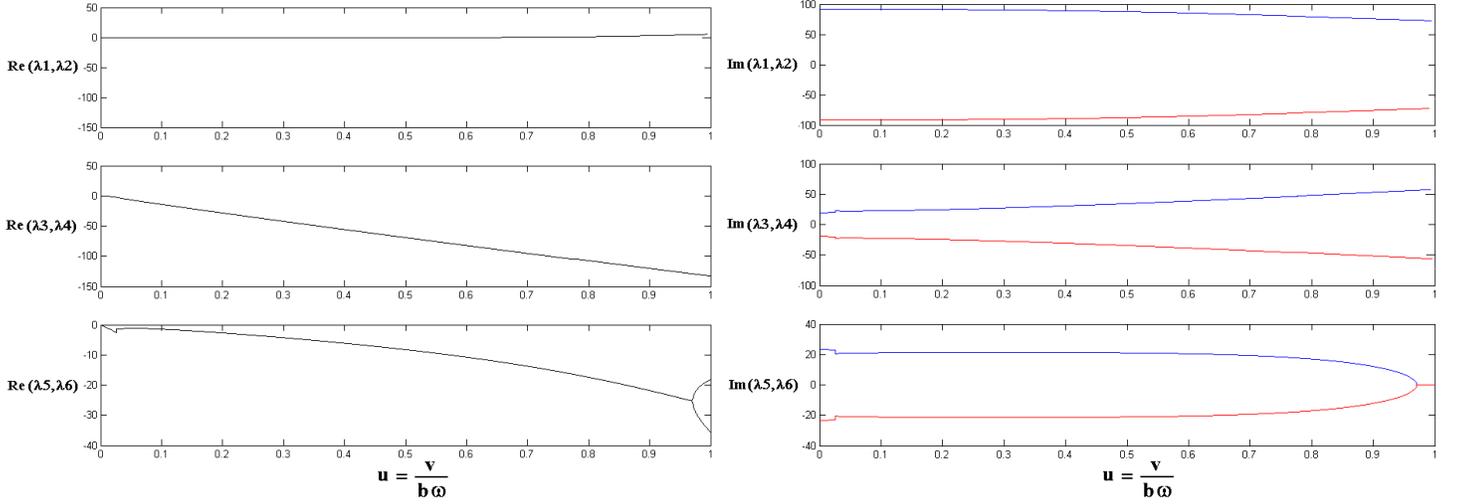
Figure 8: (a) Real part of eigenvalues plotted versus flow nondimensionalized flow speed. (b) Imaginary part of eigenvalues plotted versus nondimensionalized flow speed. The first bifurcation for $u \approx 0.65$, which corresponds to a physical speed of 108 m/s in this case.

alized constants:

$$
\begin{aligned}
\kappa &= \frac{\pi \rho_\infty b^2}{m}, \quad u_\infty = \frac{v_\infty}{b \omega_\alpha} \\
r_\alpha &= \sqrt{\frac{I_\alpha}{mb^2}}, \quad r_\beta = \sqrt{\frac{I_\beta}{mb^2}} \\
x_\alpha &= \frac{S_\alpha}{mb}, \quad x_\beta = \frac{S_\beta}{mb} \\
\omega_\alpha &= \sqrt{\frac{k_\alpha}{I_\alpha}}, \quad \omega_\beta = \sqrt{\frac{k_\beta}{I_\beta}}, \quad \omega_h = \sqrt{\frac{k_h}{m}}.
\end{aligned}
\tag{43}
$$

Defining nondimensional variables $\{\bar{\alpha}, \bar{\beta}, \bar{h}\} = \{\alpha, \beta, \frac{h}{b}\}$ and using the parameters from equations (43), we can rewrite equations (42)in nondimensional form, $[\bar{M}]\ddot{\vec{q}} + [\bar{C}]\dot{\vec{q}} + [\bar{K}]\vec{q} = \{0\}$. Written explicitly, we have the

33
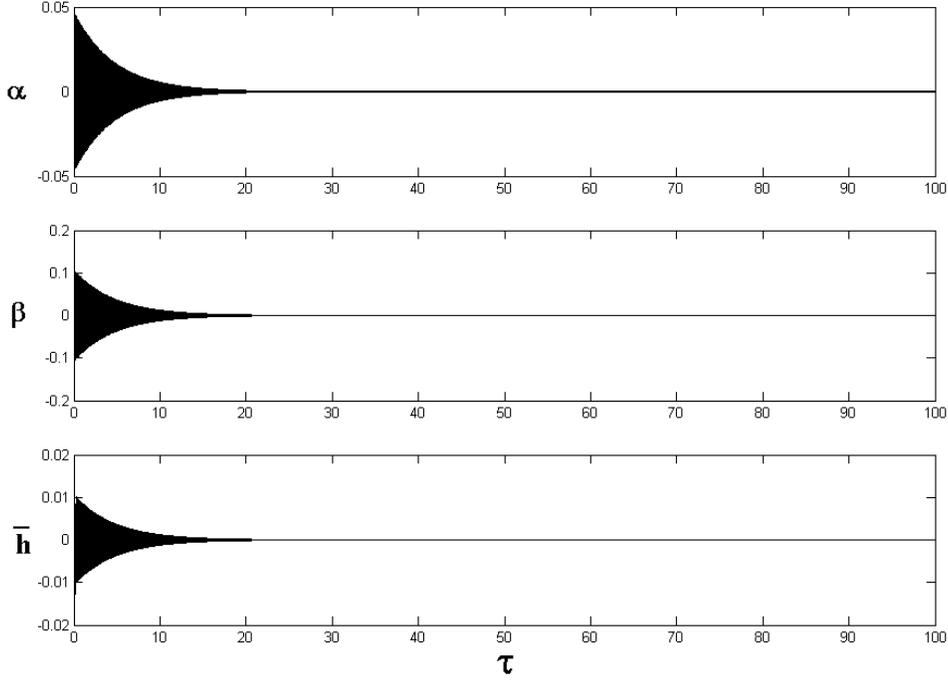
Figure 9: System dynamics for 100 nondimensional time units. Note that the oscillations decay with time because this velocity is below the flutter boundary.

following equations:

$$
\begin{bmatrix}
\frac{r_\alpha^2}{\omega_\alpha^2} + \frac{\kappa}{\omega_\alpha^2}\left(\frac{1}{8}+a^2\right) & \frac{r_\beta^2}{\omega_\alpha^2} + (c-a)\frac{x_\beta}{\omega_\alpha^2} + 2\frac{\kappa}{\omega_\alpha^2}\frac{T_{13}}{\pi} & \frac{x_\alpha}{\omega_\alpha^2} - a\kappa \\
\frac{r_\beta^2}{\omega_\alpha^2} + (c-a)\frac{x_\beta}{\omega_\alpha^2} + 2\frac{\kappa}{\omega_\alpha^2}\frac{T_{13}}{\pi} & \frac{r_\beta^2}{\omega_\alpha^2} - \frac{\kappa}{\omega_\alpha^2}\frac{T_3}{\pi^2} & \frac{x_\beta}{\omega_\alpha^2} - \frac{\kappa}{\omega_\alpha^2}\frac{T_1}{\pi} \\
\frac{x_\alpha}{\omega_\alpha^2} - a\kappa & \frac{x_\beta}{\omega_\alpha^2} - \frac{\kappa}{\omega_\alpha^2}\frac{T_1}{\pi} & 1+\kappa
\end{bmatrix}
\begin{Bmatrix} \ddot{\bar\alpha} \\ \ddot{\bar\beta} \\ \ddot{\bar h} \end{Bmatrix} +
$$

$$
\begin{bmatrix}
\left[\left(\frac{1}{2}-a\right)+2\left(a^2-\frac{1}{4}\right)C(k)\right]\frac{\kappa}{\omega_\alpha}u_\infty & \left[T_1 - T_8 - (c-a)T_4 + \frac{1}{2}T_{11} - \left(a+\frac{1}{2}\right)T_{11}C(k)\right]\frac{\kappa}{\pi\omega_\alpha}u_\infty & -2\left(a+\frac{1}{2}\right)C(k)\frac{\kappa}{\omega_\alpha}u_\infty \\
\left[T_4\left(a-\frac{1}{2}\right)-T_1-2T_9+T_{12}\left(\frac{1}{2}-a\right)C(k)\right]\frac{\kappa}{\pi\omega_\alpha}u_\infty & -\left[T_4 T_{11} - T_{11}T_{12}C(k)\right]\frac{\kappa}{2\pi^2\omega_\alpha}u_\infty & T_{12}C(k)\frac{\kappa}{\pi\omega_\alpha}u_\infty \\
\left[1+(1-2a)C(k)\right]\frac{\kappa}{\omega_\alpha}u_\infty & -(T_4 - T_{11}C(k))\frac{\kappa}{\pi\omega_\alpha}u_\infty & 2C(k)\frac{\kappa}{\omega_\alpha}u_\infty
\end{bmatrix}
\begin{Bmatrix} \dot{\bar\alpha} \\ \dot{\bar\beta} \\ \dot{\bar h} \end{Bmatrix}
$$

$$
+\begin{bmatrix}
r_\alpha^2 - 2\left(a+\frac{1}{2}\right)C(k)\kappa u_\infty^2 & \left[T_4 + T_{10} - 2\left(a+\frac{1}{2}\right)T_{10}C(k)\right]\frac{\kappa}{\pi}u_\infty^2 & 0 \\
T_{12}C(k)\rho_\infty\frac{\kappa}{\pi}u_\infty^2 & r_\beta^2 + (T_5 - T_4 T_{10} + T_{10}T_{12}C(k))\frac{\kappa}{\pi^2}u_\infty^2 & 0 \\
2C(k)\kappa u_\infty^2 & 2T_{10}C(k)\frac{\kappa}{\pi}u_\infty^2 & \frac{\omega_h^2}{\omega_\alpha^2}
\end{bmatrix}
\begin{Bmatrix} \bar\alpha \\ \bar\beta \\ \bar h \end{Bmatrix} = \begin{Bmatrix} 0 \\ 0 \\ 0 \end{Bmatrix} \tag{44}
$$

Performing the operation $\ddot{\vec{q}} = -([\bar M]^{-1}[\bar K]\vec{q} + [\bar M]^{-1}[\bar C]\dot{\vec{q}})$ and introduc-

34

ing a change of variables, $\{\bar{x}_1, \bar{x}_2, \bar{x}_3, \bar{x}_4, \bar{x}_5, \bar{x}_6\} = \{\bar{\alpha}, \bar{\beta}, \bar{h}, \dot{\bar{\alpha}}, \dot{\bar{\beta}}, \dot{\bar{h}}\}$, we write the equations as 6 linear homogenous first order ODEs in the following nondimensionalized matrix form,

$$
\left\{\begin{array}{c} \dot{\bar{x}}_1 \\ \dot{\bar{x}}_2 \\ \dot{\bar{x}}_3 \\ \dot{\bar{x}}_4 \\ \dot{\bar{x}}_5 \\ \dot{\bar{x}}_6 \end{array}\right\} = \left[\begin{array}{cccccc} 0 & 0 & 0 & 1 & 0 & 0 \\ 0 & 0 & 0 & 0 & 1 & 0 \\ 0 & 0 & 0 & 0 & 0 & 1 \\ m_{11} & m_{12} & m_{13} & n_{11} & n_{12} & n_{13} \\ m_{21} & m_{22} & m_{23} & n_{11} & n_{12} & n_{13} \\ m_{31} & m_{32} & m_{33} & n_{11} & n_{12} & n_{13} \end{array}\right] \left\{\begin{array}{c} \bar{x}_1 \\ \bar{x}_2 \\ \bar{x}_3 \\ \bar{x}_4 \\ \bar{x}_5 \\ \bar{x}_6 \end{array}\right\} \qquad (45)
$$

In the equations, m_{ij}, $i, j = 1, 2, 3$ and n_{ij}, $i, j = 1, 2, 3$ are constants that have analytical expressions in terms of the entries of the inertia $[M]$, stiffness $[K]$ and damping $[C]$ matrices. Analytical solutions of the form $\vec{\bar{x}} = \vec{\nu}_i e^{\lambda_i \tau}, i = \{1 \ldots 6\}$ were found for equations (45), where λ_i is an eigenvalue of the system with an associated eigenvector $\vec{\nu}_i$. The equations were solved numerically for the parameters given in Table 3 and the initial condition vector $\{0.05, 0.025, 0, 0, 0, 0\}$. The parameters chosen are typical for large commercial aircraft [2]. The numerical results agreed very closely with the analytical solution.

Choosing nondimensionalized velocity u (equations (43)) as the parameter, bifurcation diagrams (Figure 8) were made for the quasi-steady model. In this case, for the parameters chosen initially, the first bifurcation was noticed at a nondimensionalized velocity of around 0.65, which corresponds to a physical velocity of $108 \, m/s$. The system dynamics for a velocity below the flutter boundary are given in Figure 9. The oscillations, as expected, decay with time.

9 Cubic Structural Nonlinearities

The assumption of linearity in an aeroelastic system leads to a prediction of flutter speed, below which the system is stable and perturbations from the equilibrium flight condition die out exponentially with time. Above the flutter speed however, the system dynamics show exponentially increasing oscillations with time. These flutter speed predictions and the characteristics of the motion are affected by the nonlinearities present in the system [3]. Nonlinearities arise from both the aerodynamics and the structural dynamics of the system. We shall consider only structural nonlinearities in this paper. An aircraft structure is affected by various kinds of nonlinearities, which can classified into either distributed or concentrated nonlinearities based on the region of their action. Distributed nonlinearities arise from general deformations of the entire structure. Concentrated nonlinear phenomena, on the other hand, are localized and result from non-ideal mechanical linkages and non-elastic structural deformations. We consider a particular type of concentrated nonlinearity that can be approximated by replacing the linear springs in our model with hard and soft nonlinear springs. Linear springs exhibit the behavior represented by the solid line in the force versus displacement curves shown in Figure 10. The spring provides a resistance proportional to its linear or angular displacement, with the proportionality constant determined by Hooke's Law. A nonlinear spring on the other hand does not deform proportionally to the displacement. A hardening spring becomes stiffer with increasing displacement or twist angle as shown by the dashed curves in the figure. A softening spring, on the other hand, offers decreasing resistance as the spring is stretched. This is represented by the dotted lines in the figure. In general, these nonlinear springs can
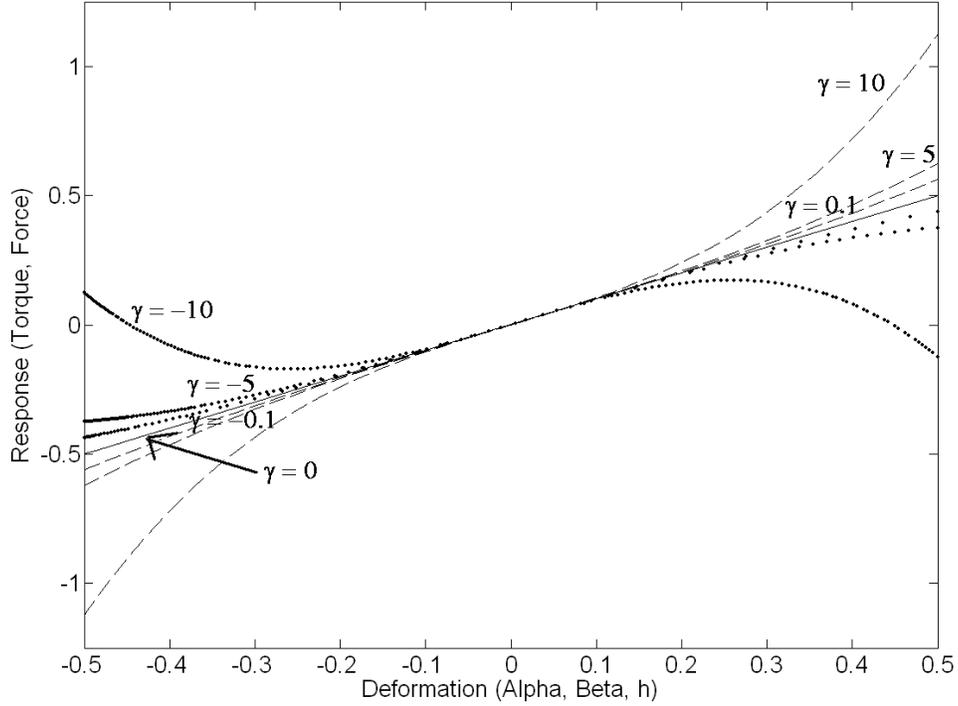
Figure 10: Behavior of cubic hardening (dashed lines) and softening springs (dotted lines) compared to a linear spring (solid line). Hardening springs become stiffer with increased displacement, while softening springs offer less resistance. The magnitude of γ indicates the degree of softness or hardness.

be represented as polynomial functions of the generalized coordinates of the system:

$$k_\alpha(\alpha) \;=\; a_0 + a_1\alpha + a_2\alpha^2 + a_3\alpha^3$$

$$k_\beta(\beta) \;=\; b_0 + b_1\beta + b_2\beta^2 + a_3\beta^3$$

$$k_h(h) \;=\; c_0 + c_1 h + c_2 h^2 + c_3 h^3$$

The constant term can be set to zero by the simple expedient of setting the initial displacement as the equilibrium position. The coefficient of the
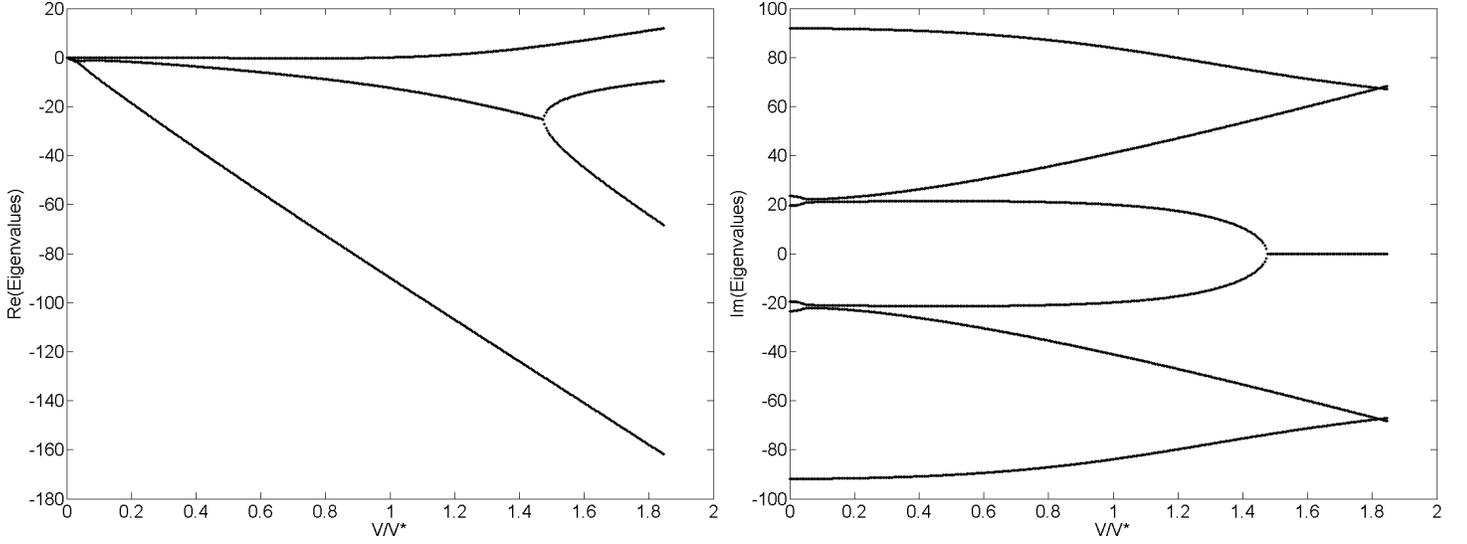
Figure 11: (a) Real part of eigenvalues plotted versus flow speed nondimensionalized with respect to flutter velocity $V*$. (b) Imaginary part of eigenvalues plotted versus nondimensionalized flow speed. The first bifurcation for $V/V* = 1$, corresponds to a physical speed of 108 m/s in this case.

square term can also be set to zero by arguing that the spring exhibits anti-symmetric behavior for loading and unloading. Then, the nonlinear springs can be represented as

$$
\begin{aligned}
k_\alpha(\alpha) &= a_1\alpha + a_3\alpha^3 \\
k_\beta(\beta) &= b_1\beta + a_3\beta^3 \\
k_h(h) &= c_1h + c_3h^3
\end{aligned}
\tag{46}
$$

For a hard spring, the coefficients of the cubic terms in the above equations are positive. The degree of hardness can be specified by defining $\gamma_1 = a_3/a_1, \gamma_2 = b_3/b_1, \gamma_3 = c_3/c_1$. Higher γ_i values correspond to harder

38
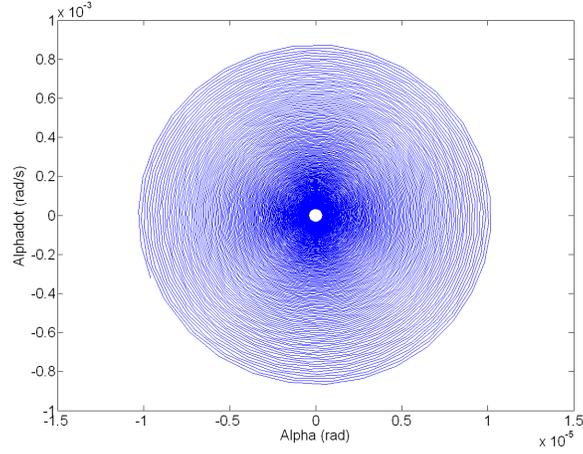
Figure 12: A phase plot of $\dot{\alpha}$ vs α shows that a very small limit cycle exists around the origin, which attracts trajectories with initial conditions outside the envelope of the limit cycle. Flow velocity is 100 m/s, which is below the predicted flutter speed of 108 m/s. The hardness coefficient $\gamma = 5$ and all other parameters are given in Table 2.

springs. For soft springs, γ_i are negative and the degree of softness is proportional to the respective magnitudes of γ_i. Replacing the constant stiffness terms in equations 12 with equations 46 above, and using the quasi-steady model from equations 41 developed in a preceding section for the aerodynamics, we obtain the following equations for an aeroelastic system with

39
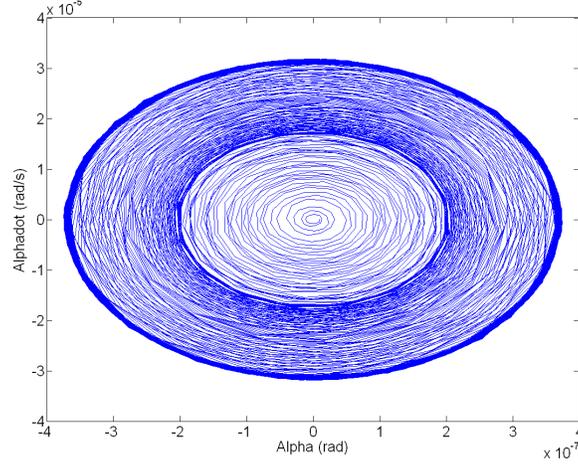
Figure 13: A phase plot of $\dot{\alpha}$ vs α shows that a very small limit cycle exists around the origin, which attracts trajectories with initial conditions inside the envelope of the limit cycle. The size of the limit cycle is 10^{-7}, which is negligible for all practical purposes. Flow velocity is 100 m/s, which is below the predicted flutter speed of 108 m/s. The hardness coefficient $\gamma = 5$ and all other parameters are given in Table 2.

cubic stiffness nonlinearities oscillating in quasi-steady flow.

$$I_\alpha\ddot{\alpha} + (I_\beta + b(c-a)S_\beta)\ddot{\beta} + S_\alpha\ddot{h} + a_1\alpha + a_3\alpha^3 = -\rho_\infty b^2\left[\pi b^2\left(\frac{1}{8}+a^2\right)\ddot{\alpha} - (T_7+(c-a)T_1)\,b^2\ddot{\beta} - \pi ab\ddot{h}\right] -$$

$$\rho_\infty b^2\left[\left(\frac{1}{2}-a\right)\pi bv_\infty\dot{\alpha} + \left(T_1 - T_8 - (c-a)T_4 + \frac{1}{2}T_{11}\right)bv_\infty\dot{\beta} + (T_4+T_{10})v_\infty^2\beta\right] +$$

$$2\pi\rho_\infty\left(a+\frac{1}{2}\right)b^2v_\infty\left[b\left(\frac{1}{2}-a\right)\dot{\alpha} + \frac{T_{11}}{2\pi}b\dot{\beta} + \dot{h} + v_\infty\alpha + \frac{T_{10}}{\pi}v_\infty\beta\right]$$

$$I_\beta\ddot{\beta} + (I_\beta + b(c-a)S_\beta)\ddot{\alpha} + S_\beta\ddot{h} + b_1\beta + a_3\beta^3 = -\rho_\infty b^2\left[2T_{13}b^2\ddot{\alpha} - \frac{T_3}{\pi}b^2\ddot{\beta} - T_1b\ddot{h}\right] -$$

$$\rho_\infty b^2\left[\left\{T_4\left(a-\frac{1}{2}\right) - T_1 - 2T_9\right\}bv_\infty\dot{\alpha} - \frac{T_4T_{11}}{2\pi}bv_\infty\dot{\beta} + \left(\frac{T_5 - T_4T_{10}}{\pi}\right)v_\infty^2\beta\right] -$$

$$T_{12}\rho_\infty b^2v_\infty\left[b\left(\frac{1}{2}-a\right)\dot{\alpha} + \frac{T_{11}}{2\pi}b\dot{\beta} + \dot{h} + v_\infty\alpha + \frac{T_{10}}{\pi}v_\infty\beta\right] \quad (47)$$

$$m\ddot{h} + S_\alpha\ddot{\alpha} + S_\beta\ddot{\beta} + c_1h + c_3h^3 = -\rho_\infty b^2\left[-\pi ab\ddot{\alpha} - T_1b\ddot{\beta} + \pi\ddot{h} + \pi v_\infty\dot{\alpha} - T_4v_\infty\dot{\beta}\right] -$$

$$2\pi\rho_\infty bv_\infty\left[b\left(\frac{1}{2}-a\right)\dot{\alpha} + \frac{T_{11}}{2\pi}b\dot{\beta} + \dot{h} + v_\infty\alpha + \frac{T_{10}}{\pi}v_\infty\beta\right]$$
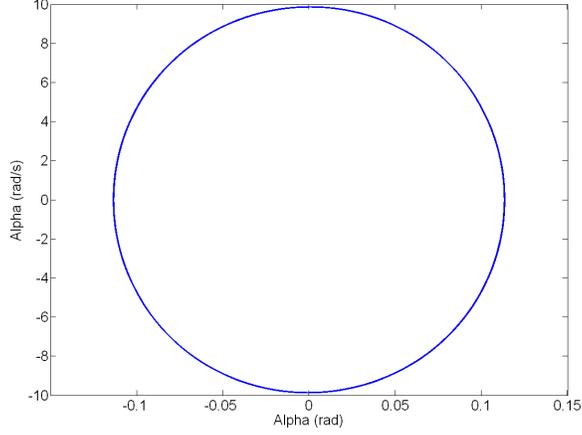
Figure 14: A phase plot of $\dot{\alpha}$ vs α shows that trajectories starting near the origin settle down to an attracting limit cycle. Flow velocity is 110 m/s, which is just above the predicted flutter speed of 108 m/s. The hardness coefficient $\gamma = 5$ and all other parameters are given in Table 2.

Note that $C(k)$ was set to 1 to correspond to quasi-steady flow. This system can then be rewritten as six first order equations of the general form:

$$
\begin{aligned}
\dot{x}_1 &= x_4 \\
\dot{x}_2 &= x_5 \\
\dot{x}_3 &= x_6 \\
\dot{x}_4 &= p_1 x_1 + p_2 x_1^3 + q_1 x_2 + q_2 x_2^3 + r_1 x_3 + r_2 x_3^3 + s_1 x_4 + s_2 x_5 + s_3 x_6; \\
\dot{x}_5 &= p_3 x_1 + p_4 x_1^3 + q_3 x_2 + q_4 x_2^3 + r_3 x_3 + r_4 x_3^3 + s_4 x_4 + s_5 x_5 + s_6 x_6; \\
\dot{x}_6 &= p_5 x_1 + p_6 x_1^3 + q_5 x_2 + q_6 x_2^3 + r_5 x_3 + r_6 x_3^3 + s_7 x_4 + s_8 x_5 + s_9 x_6;
\end{aligned}
\tag{48}
$$

Here, p_i, q_i, r_i, and s_j, $i = \{1, \ldots, 6\}$ and $j = \{1, \ldots, 9\}$ are constants expressed analytically in terms of the system parameters defined in equations 43 and the airstream velocity v_∞. Linear stability analysis was done by constructing the following Jacobian matrix for a general fixed point

41
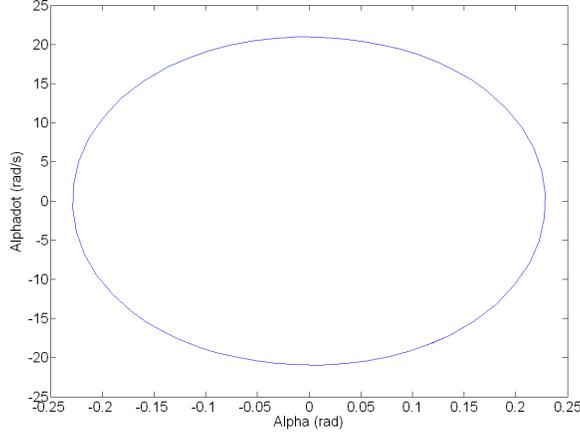
Figure 15: Comparing this phase plot of $\dot{\alpha}$ vs α with that of Figure 14 shows that the amplitude of the limit cycle has grown as the velocity has increased. Flow velocity is 150 m/s, which is above the predicted flutter speed of 108 m/s. The hardness coefficient $\gamma = 5$ and all other parameters are given in Table 2.

$\vec{x}_i^* = (x_1^*, x_2^*, x_3^*, x_4^*, x_5^*, x_6^*).$

$$
Df(\vec{x}_i^*) = \begin{bmatrix} 0 & 0 & 0 & 1 & 0 & 0 \\ 0 & 0 & 0 & 0 & 1 & 0 \\ 0 & 0 & 0 & 0 & 0 & 1 \\ p_1 + 2p_2 x_1^2 & q_1 + 2q_2 x_2^2 & r_1 + 2r_2 x_3^2 & s_1 & s_2 & s_3 \\ p_3 + 2p_4 x_1^2 & q_3 + 2q_4 x_2^2 & r_3 + 2r_4 x_3^2 & s_4 & s_5 & s_6 \\ p_5 + 2p_6 x_1^2 & q_5 + 2q_6 x_2^2 & r_5 + 2r_6 x_3^2 & s_7 & s_8 & s_9 \end{bmatrix}_{\vec{x}_i^*} \tag{49}
$$

10   Cubic Hardening Springs

An aeroelastic system with cubic hardening springs can be described by equations 47with positive cubic coefficients. The only physical fixed point for this case is the origin, $(0, 0, 0, 0, 0, 0)$. The eigenvalues of the Jacobian

42
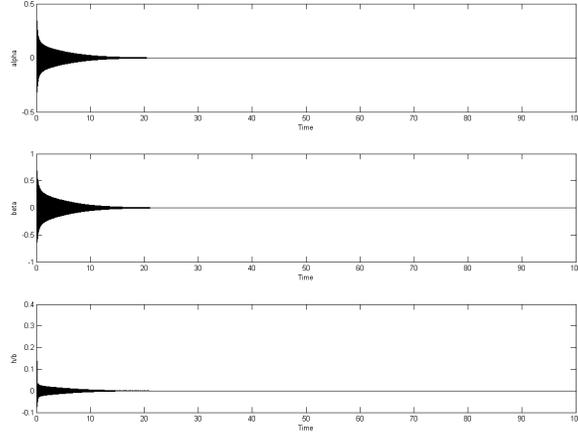
Figure 16: This time series plot shows the oscillations with exponentially decreasing amplitude for a speed of 100 m/s, which is below the predicted flutter speed of 108 m/s. The hardness coefficient $\gamma = 5$ and all other parameters are given in Table 2.
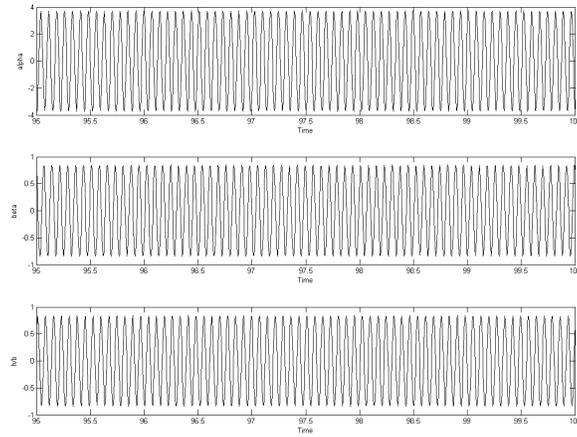
Figure 17: This time series plot shows limit cycle oscillations with for a speed of 150 m/s, which is above the predicted flutter speed of 108 m/s. The hardness coefficient $\gamma = 5$ and all other parameters are given in Table 2.

43
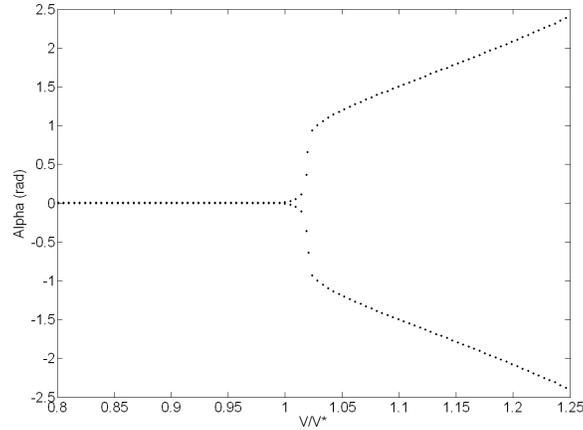
Figure 18: This plot shows the growth of the limit cycle amplitude with change in speed nondimensionalized with respect to flutter speed $V*$. The hardness coefficient $\gamma = 0.05$ and all other parameters are given in Table 2. The limit cycle amplitude is 285° at a speed 25% greater than flutter, clearly indicating that the airfoil has undergone catastrophic oscillations at this point.

evaluated at this fixed point have negative real parts for values less than the flutter speed, V^*. The flutter speed is predicted from the linear system as described in section 6. Bifurcation diagrams for the eigenvalues of the system for the dimensionless parameter $V/V*$ are shown in Figure 11. For values of $V/V^* < 1$ the airspeed velocity is less than the flutter speed and the system is asymptotically stable. For values above this dimensionless speed, exponentially divergent oscillations are predicted by the linearization. This predicted behavior is similar to the quasi-steady linear case presented in section 8. The system behavior was investigated for a range of velocities using numerical simulations for various hardness values. The effect of the elastic center location was also investigated.

44
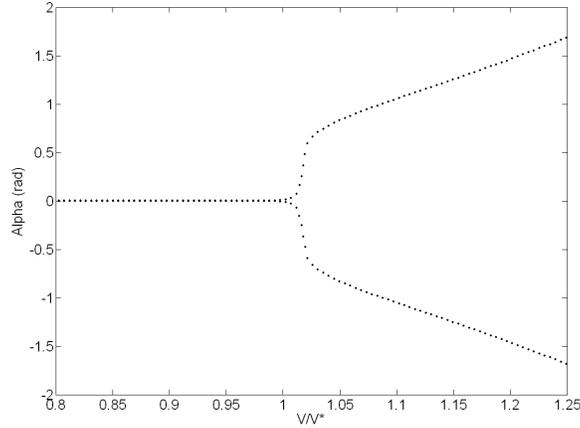
Figure 19: This plot shows the growth of the limit cycle amplitude with change in speed nondimensionalized with respect to flutter speed $V*$. The hardness coefficient $\gamma = 0.1$ and all other parameters are given in Table 2. The limit cycle amplitude is $200°$ at a speed 25% greater than flutter, which is lower than the previous case where $\gamma = 0.1$. However, this is still a catastrophic case of flutter.

For speeds below the onset of flutter, a very small attracting limit cycle surrounds the origin. This is shown in Figures 12, where the trajectory was started close to the origin, but outside the envelope of the limit cycle. For a set of initial conditions outside the closed orbit, trajectories spiral inwards to the limit cycle. Figure 13 shows a trajectory that was started very close to the origin, which approaches the limit cycle from the inside. The system dynamics for speeds below flutter exponentially decrease to the amplitude of the limit cycle, of the order 10^{-7} which is for all practical purposes zero. For speeds above the flutter speed however, the limit cycle increases in size proportional to the airspeed velocity. This behavior is shown in Figures 14 and 15. The spring hardness for the example shown is $\gamma_i = 5$ and the other

45
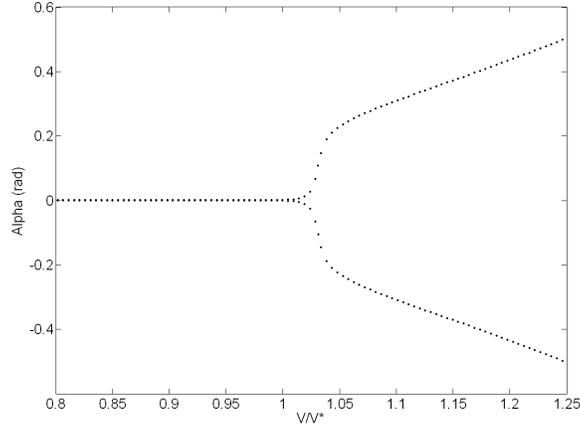
Figure 20: This plot shows the growth of the limit cycle amplitude with change in speed nondimensionalized with respect to flutter speed $V*$. The hardness coefficient $\gamma = 1$, which implies that the linear terms are equal in magnitude to the nonlinear terms. All other parameters are given in Table 2. The limit cycle amplitude is $60°$ at a speed 25% greater than flutter, which is quite severe, but the amplitude has decreased significantly.

parameters are the same as before (see Table 2). Time series of α oscillations are shown in Figure 16 for a speed of 100 m/s, which shows exponentially decreasing oscillations. At a speed of 150 m/s, around 40 m/s above the flutter speed, the system settles down to a limit cycle oscillation as shown in Figure 17.

The size of the limit cycle also depends on the hardness of the spring. Figures 18 through 22 show plots of the limit cycle amplitude versus the non-dimensional speed $V/V*$, where $V*$ is the flutter speed predicted by the linear quasi-steady model. The spring hardness coefficient $\gamma_i = 0.05, 0.1, 1, 5$, and 10 respectively. For small values of γ_i, the limit cycle amplitude grows to values greater than $90°$, which indicates catastrophic wing failure, for speeds
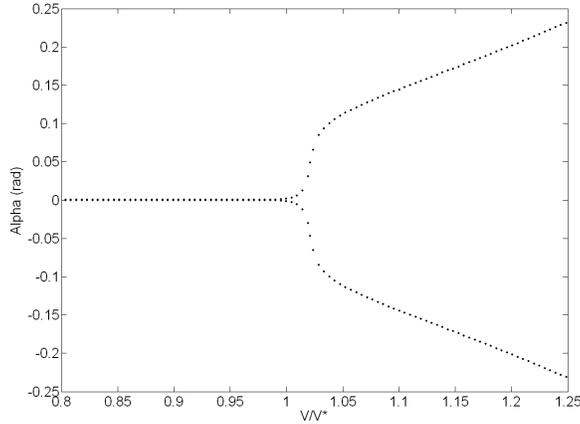
Figure 21: This plot shows the growth of the limit cycle amplitude with change in speed nondimensionalized with respect to flutter speed $V*$. The hardness coefficient $\gamma = 5$. For the first time, the system has nonlinearities that are larger than the linear terms. All other parameters are given in Table 2. The limit cycle amplitude is $25°$ at a speed 25% greater than flutter. This is a big improvement over all the other cases, but can still be cause for concern in the design of a wing.

only 25% above the flutter speed. As the spring hardness is increased to a value $\gamma > 1$, at which point the nonlinear term is larger than the linear term, the amplitude of oscillations is reduced to a more reasonable $20°$. For all cases, the limit cycle starts to grow in amplitude exactly at the flutter speed predicted by the linearized model.

Changing the elastic axis position (a in Figure˜refairfoil) has a dramatic affect on the linearly predicted flutter velocity. For values of $a > -0.5$, the system exhibits instability for all speeds. For this reason, this particular airfoil was designed with an elastic axis at $a = -0.5$. Moving the elastic axis to $a = -0.6$ increases the flutter velocity to $129m/s$. It also has an

47
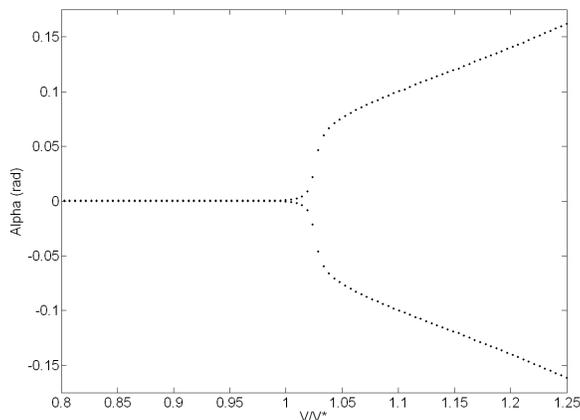
Figure 22: This plot shows the growth of the limit cycle amplitude with change in speed nondimensionalized with respect to flutter speed $V*$. The hardness coefficient $\gamma = 10$ and all other parameters are given in Table 2. The limit cycle amplitude is 15° at a speed 25% greater than flutter. This is within acceptable limits for large wings.

affect on the amplitude of the limit cycle oscillations induced after the flutter. Comparing Figures̃refhardlco5 and 23 shows that the amplitude of the oscillations has reduced by 33% at a speed 25% greater than flutter speed for the same spring hardness coefficient by moving the elastic axis forward by 20%. In fact, the amplitude of the limit cycle is comparable to that of a much harder spring with $\gamma = 10$, shown in Figure 22.

11   Concluding Remarks

In this paper, we derived a linear steady state aeroelastic model in three DOF for an airfoil with two spatial dimensions. We derived equations of motion from the Lagrangian formulation for conservative systems. A flutter boundary was predicted at sea level conditions and the effects of airfoil
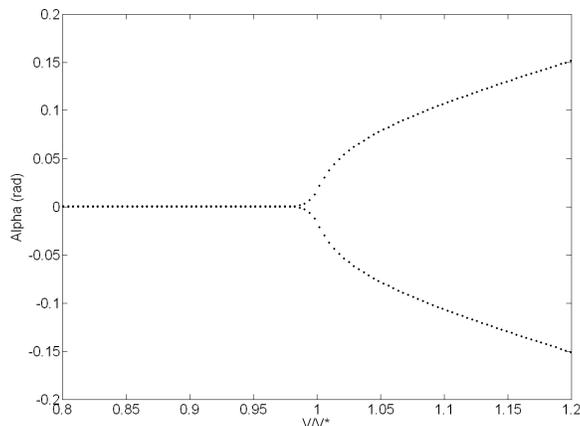
Figure 23: This plot shows the decrease in the limit cycle amplitude with change in the position of the elastic axis to $a = -0.6$ from -0.5 (see Figure~refairfoil). The hardness coefficient $\gamma = 5$ and all other parameters are given in Table 2. The limit cycle amplitude is $17°$ at a speed 25% greater than flutter. This is comparable to the case of $\gamma = 10$.

geometry and structural characteristics on the predicted value were studied. The results indicate that a linear steady state model cannot accurately predict the flutter boundary. A major weakness of the model lies in the assumed steadiness of the airflow around an airfoil. The airfoil-flow interactions produce perturbations that are entirely neglected in a non-dissipative model. Furthermore, the steady state assumption limits the velocity range for which this model is valid, due to the necessary limitations of inviscidity and incompressibility that have been introduced while deriving the aerodynamical model. However, the model does provide a certain amount of insight into the nature of the flutter boundary. We have shown that the flutter boundary can be inferred from the behavior of the real part of the eigenvalues arising from the equations of motion. It has also been noticed

49

that changing certain airfoil structural and geometrical parameters leads to a shift in the position of the flutter boundary. This is significant because it allows for the design of an airfoil which will never encounter flutter for a certain flight regime.

We then developed a quasi-steady aerodynamic model, which is a better representation of real flow around an airfoil. The introduction of dissipative forces into the flow around an airfoil led to a more realistic prediction of flutter characteristics. We have adopted Theodorsen's unsteady thin airfoil theory [2] as our aerodynamic model. The theory is modified by assuming a slowly changing flow, leading to the quasi-steady form of Theodorsen's theory. The aerodynamic forcing functions are expressed as functions of time derivatives of the system variables. This was combined with the structural dynamics to complete the dissipative aeroelastic model.

In the next step we incorporate structural nonlinearities into the unsteady model by replacing the structural stiffness constants k_α, k_β, k_h with polynomial stiffness coefficients $k_\alpha(\alpha), k_\beta(\beta), k_h(h)$. We studied a particular kind of structural nonlinearity, which can be modeled using cubic hardening springs of the general form $s_1 q + s_{(}3)q^3$, where q is a system variable. The model predicts a very small attractive limit cycle enclosing the origin, which makes the system settle down to oscillations of negligible amplitude at speeds before the flutter velocity. At the linearly predicted flutter velocity, however, the limit cycle grows in size. The amplitude of the limit cycle oscillations increases with the airspeed. A system with a larger cubic hardness coefficient undergoes smaller amplitude oscillations when compared to a system with smaller nonlinearities at the same speed. The amplitude of the limit cycles also decreases when the elastic center is moved forward towards the leading edge of the airfoil.

Acknowledgements

References

[1] Dewey H. Hodges and G. Alvin Pierce. *Introduction to Structural Dynamics and Aeroelasticity*. Cambridge University Press, first edition, 2002.

[2] Theodore Theodorsen. General theory of aerodynamic instability and the mechanism of flutter. NACA Technical Report 496, 1935.

[3] B.H.K. Lee, S.J. Price, and Y.S. Wong. Nonlinear aeroelastic analysis of airfoils: bifurcation and chaos. *Progress in Aerospace Sciences*, (35):205–334, 1999.

[4] John D. Anderson Jr. *Fundamentals of Aerodynamics*. McGraw-Hill, third edition, 2001.

[5] Ira H. Abbott and Albert E. von Doenhoff. *Theory of Wing Sections*. Dover Publications, first edition, 1959.

[6] Herbert Goldstein, Charles P. Poole Jr, and John L. Safko. *Classical Mechanics*. Addison Wesley, third edition, 2003.

[7] Frank M. White. *Fluid Mechanics*. McGraw-Hill, fifth edition, 2002.

[8] Arnold M. Kuethe and Chuen-Yen Chow. *Foundations of Aerodynamics - Bases of Aerodynamic Design.* John Wiley and Sons, fifth edition, 1998.

[9] Hermann Glauert. Theoretical relationships for an aerofoil with hinged flap. ARC Reports and Memoranda 1095, Aeronautical Research Committee, 1927.

[10] E.H. Dowell, J.P. Thomas, and K.C. Hall. Transonic limit cycle oscillation analysis using reduced order aerodynamic models. *Journal of Fluids and Structures*, (19):17–27, 2004.

[11] John D. Anderson Jr. *Aircraft Performance and Design.* McGraw-Hill International Editions, international edition, 1999.

[12] L.D. Landau and E.M. Lifshitz. *Mechanics*, volume 1 of *Course of Theoretical Physics.* Butterworth Heinemann, third edition, 2001.

Appendix

The length of the flap chord, from Figure 1 is $b_f = b(1 - c)$. We define the constant nondimensional parameter $E = \frac{b_f}{b} = 1 - c$. Then we can express the partial derivatives σ_i, $i = \{1 \ldots 6\}$, used in the equations $(29, 34, \text{and } 36)$ of the steady aerodynamic model (see section 5), solely in terms of E as follows:

$$
\begin{aligned}
\sigma_1 &= \frac{\partial c_l}{\partial \alpha} = 2\,\pi \\[6pt]
\sigma_2 &= \frac{\partial c_l}{\partial \beta} = \sigma_1 \left[1 - \frac{2}{\pi} \left(\arccos(\sqrt{E}) - \sqrt{E(1-E)} \right) \right] \\[6pt]
\sigma_3 &= \frac{\partial c_{m,ac}}{\partial \alpha} = 0 \\[6pt]
\sigma_4 &= \frac{\partial c_{m,ac}}{\partial \beta} = -\frac{1}{2}(2-E)\sqrt{E(2-E)} \\[6pt]
\sigma_5 &= \frac{\partial c_{m,\alpha}}{\partial \alpha} = -\frac{1}{4}\sigma_1 \\[6pt]
\sigma_6 &= \frac{\partial c_{m,\alpha}}{\partial \beta} = -\frac{1}{4}\sigma_2 - 2(1-E)\sqrt{E(1-E)} \\[6pt]
\sigma_7 &= \frac{\partial c_{m,\beta}}{\partial \alpha} = -\frac{4\sigma_1}{\pi E^2} \left[\left(\frac{3}{2}-E\right)\sqrt{E(1-E)} - \left(\frac{3}{2}-2E\right)\left(\frac{\pi}{2}-\arccos(\sqrt{E})\right) \right] \\[6pt]
\sigma_8 &= \frac{\partial c_{m,\beta}}{\partial \beta} = \frac{\sigma_7\sigma_2}{\sigma_1} - \frac{2(1-E)\sqrt{E(1-E)}}{\pi E^2} \left[\frac{\pi}{2} - \arccos(\sqrt{E}) - \sqrt{E(1-E)} \right]
\end{aligned}
\tag{50}
$$

The Theodorsen unsteady aerodynamic theory [2] derives the following constants T_i, $i = \{1\ldots 14\}$ in terms of the constant airfoil length c (see Figure 1). The constants appear in the equations (41, 42, and 44) in the section 8, wherein we derive the linear quasi-steady aerodynamic model.

$$
\begin{aligned}
T_1 &= c\,\arccos(c) - \frac{1}{3}(2+c^2)\sqrt{1-c^2} \\
T_2 &= c\,(1-c^2) - (1+c^2)\sqrt{1-c^2}\,\arccos(c) + (c\,\arccos(c))^2 \\
T_3 &= \frac{1}{4}c\,(7+2c^2)\sqrt{1-c^2}\,\arccos(c) - \left(\frac{1}{8}+c^2\right)(\arccos(c))^2 - \frac{1}{8}(1-c^2)(5c^2+4) \\
T_4 &= c\,\sqrt{1-c^2} - \arccos(c) \\
T_5 &= 2\,c\,\sqrt{1-c^2}\,\arccos(c) - (\arccos(c))^2 + c^2 - 1 \\
T_6 &= T_2 \\
T_7 &= \frac{1}{8}c\,(2c^2+7)\sqrt{1-c^2} - \left(\frac{1}{8}+c^2\right)\arccos(c) \\
T_8 &= c\,\arccos(c) - \frac{1}{3}(2c^2+1)\sqrt{1-c^2} \\
T_9 &= \frac{1}{2}\left[\frac{1}{3}\sqrt{(1-c^2)^3} + aT_4\right] \\
T_{10} &= \sqrt{1-c^2} + \arccos(c) \\
T_{11} &= (1-2c)\arccos(c) + (2-c)\sqrt{1-c^2} \\
T_{12} &= (2+c)\sqrt{1-c^2} - (2c+1)\arccos(c) \\
T_{13} &= -\frac{1}{2}\left[T_7 + (c-a)T_1\right] \\
T_{14} &= \frac{1}{16} + \frac{1}{2}ac
\end{aligned}
\tag{51}
$$